AN ELECTROMAGNETIC MEMS-BASED RESONATOR DESIGN FOR CATHETER TRACKING IN MRI

by

Ahmet Uraz Çakacı

B.S, Electrical and Electronics Engineering, Boğaziçi University, 2010

Submitted to the Institute for Graduate Studies in
Science and Engineering in partial fulfillment of
the requirements for the degree of
Master of Science

Graduate Program in Electrical and Electronics Engineering
Boğaziçi University

2013

ACKNOWLEDGEMENTS

First of all, I would like to express my gratitude to my thesis supervisor Prof. Arda Deniz Yalçınkaya for giving me an opportunity to be a part of this beautiful project. His guidance, support, and kindness throughout this study was extremely valuable for me.

Secondly, I am grateful to Prof. Hamdi Torun for helping me in almost all stages of my study. The precious time he spend for this study is very important to me. I would also like to thank Prof. Çetin Yılmaz for joining to my thesis committee and for his valuable contributions in the analytical parts of my thesis.

I want to show my appreciation to Mustafa Kemal Ruhi and Mehmet Yumak for helping me in the fabrication process in cleanroom. I am especially grateful to Mustafa for his friendship and for teaching me almost everything I know about working in a cleanroom. In addition, I want to thank Mohammad Hossein Mazaheri Kouhani for his contributions and for being a good friend.

I would also like to thank The Scientific and Technological Research Council of Turkey (TÜBİTAK) for providing scholarship throughout my study. This project is supported by TÜBİTAK, grant EEEAG 111E197.

Finally, I owe my deepest gratitude to every special and precious person in my life, as my family and as my friend. Thank you all...

ABSTRACT

AN ELECTROMAGNETIC MEMS-BASED RESONATOR DESIGN FOR CATHETER TRACKING IN MRI

Using Magnetic Resonance Imaging (MRI) in minimally invasive medical procedures has many advantages, such as the elimination of ionizing radiation and increased soft tissue contrast. However, the lack of MRI-compatible catheters is a significant issue for MRI-based endovascular applications. In this thesis, we present design, fabrication, and characterization of MEMS resonator structures, which are intended to be used in a catheter tracking system for MRI. The actuation mechanism is based on Lorentz force, where a driving current carries the position information for the catheter. Novelty of this work is the utilization of the huge DC magnetic field present in MRI for actuation, which leads to a low-power solution. Moreover, using optical techniques to transfer the signal to the outside of the MRI environment eliminates the use of metal wires, which cause heating problem in MRI. We designed devices for two different optical readout methods, namely laser Doppler vibrometry (LDV) and diffraction grating interferometry (DGI). The necessary theoretical background for the design along with the analytical calculations is given in this thesis. Dynamic characteristics of resonators are also investigated by FEA simulations. A three-mask procedure is developed to fabricate the devices and the details of the fabrication process in cleanroom are explained. We achieved to define grating elements with 4 μm period and 50 % fill factor, which is the highest resolution required for the fabrication of the devices. In characterization stage, the dynamic characteristics of the fabricated devices are obtained. The results show that the devices can indeed be actuated by Lorentz force and the produced mechanical signal can be detected using optical methods. We measured the signal-to-noise ratio to be at least 20 throughout the frequency range of interest, for 0.13 T magnetic field strength and 0.4 mA rms driving current.

ÖZET

MRG İÇİN KATETER TAKİBİ AMAÇLI ELEKTROMANYETİK MEMS-TABANLI RESONATÖR TASARIMI

Damar içi tıbbi müdahaleri manyetik rezonans görüntüleme (MRG) altında yapmak birçok açıdan avantajlıdır. Bu konuda, MRG uyumlu kateterlerin eksikliği önemli bir sorundur. Bu tez çalışmasında, MRG uyumlu kateter takibi amacıyla geliştirilen MEMS rezonatör yapılarının tasarım, üretim ve karakterizasyonuna değineceğiz. Bu yapılar için tahrik mekanizması Lorentz kuvvetine dayanmaktadır. Kuvveti oluşturan akım kateterin yer bilgisini taşımaktadır. Bu çalışmanın asıl özgün yönü ise tahrik mekanizmasında MRG cihazı içerisindeki manyetik alandan faydalanılmasıdır. Bu halihazırda var olan çok güçlü manyetik alanın kullanılması düşük güç kullanımının önünü açmaktadır. Bununla birlikte, MRG dışına sinyalleri optik yöntemlerle aktarmak, metal kablo kullanımını önleyerek, bu hatlardaki ısınma probleminin önüne geçmektedir. Bu çalışmada lazer Doppler titreşimölçümü ve kırınım ızgarası girişimölçümü yöntemleri üzerinde durulmaktadır. Bu konuda gerekli teorik bilgi tezde verilmiştir. Yapıların dinamik özellikleri sonlu eleman analizi simülasyonları ile incelenmiştir. Üç maskeli bir üretim süreci geliştirilmiş ve temizodadaki süreç açıklanmıştır. Sonuç olarak bizim için gerekli en yüksek ayrıntı seviyesi olan 4 μm periyot ve %50 boşluk değerine sahip kırınım ızgaraları başarıyla üretilmiştir. Karakterizasyon aşamasında yapıların dinamik karakterleri tespit edilmiştir. Sonuçlar yapıların elektromanyetik tahrik mekanizması ile çalışabildiklerini ve bunun optik olarak algılanabildiğini göstermektedir. İlgilenilen frekans aralığında, 0.13 T manyetik alan ve 0.4 mA rms akımı için, işaret-gürültü oranı 20 üstü olarak ölçülmüştür.

TABLE OF CONTENTS

LIST OF FIGURES

LIST OF TABLES

LIST OF SYMBOLS

A	Cross sectional area
B_0	DC magnetic field
B_{Grad}	Gradient magnetic field
c	Coefficient of damping force
c_d	Viscous damping coefficient for squeeze film damping
E	Young's modulus
F_0	Supporting force
F_d	Driving force amplitude
f_{dr}	Driving force function
f_{FID}	Larmor frequency
f_{Larmor}	Larmor frequency
F_L	Lorentz force
f_{res}	Resonant frequency
F_T	Counteracting force due to tensile stress
g	Gravitational acceleration
i	Electrical current
I	Moment of inertia
I_{in}	Incident light intensity
I_n	Intensity of reflected diffraction orders
k	Spring constant
k_e	Spring constant of elastic damping force
k_T	Spring constant due to tensile stress
l_r	Resonator length
m	Mass
M	Bending moment
m_0	Restrictive moment
M_t	Total mass
M_{XY}	Net magnetization in transverse direction

M_Z	Net magnetization in longitudinal
n	Coefficient of damping
R	Photodetector responsivity
v	Velocity
w	Displacement function in the out-of-plane direction
w_{eff}	Effective width
α	Equalizing gain
α_{Al}	Thermal expansion coefficient for aluminum
α_{Si}	Thermal expansion coefficient for silicon
γ	Gyromagnetic ratio
ΔL_r	Relative elongation
Δp	Pressure change
ΔT	Temperature change
λ	Wavelength of light
ρ	Density of the material
σ_T	Tensile stress
ω	Angular frequency
ω_0	Natural vibration frequency
ω_c	Cut-off frequency of squeeze film damping
ω_{res}	Resonant frequency

LIST OF ACRONYMS/ABBREVIATIONS

2D	Two Dimensional
3D	Three Dimensional
AC	Alternating Current
CMOS	Complementary Metal Oxide Semiconductor
CT	Computed Tomography
DC	Direct Current
DGI	Diffraction Grating Interferometry
FEA	Finite Element Analysis
FID	Free Induction Decay
HMDS	Hexamethyldisilazane
LDV	Laser Doppler Vibrometry
MEMS	Micro Electro Mechanical Systems
MRI	Magnetic Resonance Imaging
RF	Radio Frequency
TMAC	Tangential Momentum Accommodation Coefficient
XF	X-Ray Fluoroscopy

1. INTRODUCTION

Minimally invasive diagnosis and treatment methods are very advantageous, when they are compared to their traditional counterparts, which involve cutting all tissues starting from the skin to the target one. Among many minimally invasive medical techniques, catheter based endovascular applications form a very important group and they are becoming more and more common with new developments [1]. Catheters are biocompatible devices, which can be inserted to the body via certain ducts or blood vessels to perform various medical procedures. One extremely important point about the minimally invasive surgical operations which involve catheters is that the location of the catheter inside the body should be known with a very high accuracy.

There are several commonly used medical imaging methods, such as ultrasound imaging (US), X-ray fluoroscopy (XF), computed tomography (CT), and magnetic resonance imaging (MRI). Among these methods, XF is widely used for catheter based endovascular applications [1]. However, there are many problems associated with using XF imaging method. The most significant problem is that the patients are exposed to ionizing radiation during the imaging procedure [2, 3]. Although the medical staff can be protected from the radiation by wearing copper vests during the operations, these heavy vests cause orthopedic complications. In addition to this, the accumulation of small doses of radiation in time can lead to health problems.

MRI is more advantageous than XF in terms of many aspects. First of all, MRI does not utilize ionizing radiation, which causes the problems that we mentioned for XF [4]. Secondly, MRI has much better soft tissue contrast and the contrast agents used in MRI are less toxic than the ones used in XF. Finally, MRI has the capability of producing three-dimensional (3D) images; whereas most XF systems produce two-dimensional (2D) ones, because they are acquired by projection operation [5,6]. There are many publications in the literature about minimally invasive operations which utilize MRI [7–25].

Although MRI has many advantages, the lack of MRI-compatible catheters prevents it from being the ultimate imaging choice for minimally invasive operations. The strong radio frequency (RF) pulses in MRI cause heating problems for conductive wires, which can be on dangerous levels for the patient [26–30]. On the other hand, the catheters which are made of materials that are not affected by RF pulses are very hard to detect in the final image.

This thesis work is a part of a TÜBİTAK project (grant EEEAG 111E197), which tries to realize an interventional MRI compatible catheter tracking system. Before going any further, it is essential for the reader to understand the basic working principles of MRI [31] and how these can be related to determining the position of the catheter.

In MRI, an image is constructed by using the electromagnetic radiation, which is emitted by stimulated nuclear magnetic dipoles in the presence of an external magnetic field. Although any nucleus with non-zero magnetic moment can be chosen for imaging, Hydrogen (H) nuclei are used; since they are abundant in human body and emit relatively strong signals. When there is no external magnetic field in MRI machine, the net magnetization of H dipoles is zero, because they are randomly oriented. When the external DC magnetic field is activated, some of H dipoles align with the field and precess with respect to it. The frequency of precession, called the Larmor Frequency (f_{Larmor}), depends on the external field strength (B_0) and the gyromagnetic ratio of the nucleus (γ) according to Equation 1.1.

$$f_{\text{Larmor}} = \gamma B_0 \tag{1.1}$$

Gyromagnetic ratio for H is 42.6 MHz/T. The alignment of H dipoles causes a nonzero magnetic moment (M_Z) parallel to the direction of the field (longitudinal direction). However, the net magnetization (M_{XY}) in the transverse direction (perpendicular to the external field) is still zero, because the phase of precession is random for every H dipole.

When H dipoles are excited by applying an RF pulse at their resonant frequency, which is equal to the Larmor frequency; some of them align against the external field and gain phase coherency. As a result of these, the net magnetization is flipped onto the transverse plane. While H dipoles return to their equilibrium state, M_{XY} decays due to dephasing. The emitted signal during this process is called free induction decay (FID) signal, which is a decaying sinusoidal at Larmor frequency. The rate of decay depends on the type of the tissue.

In order to determine the position of the FID signal, gradient magnetic fields (B_{Grad}), whose strength is a function of the position, are added to the external DC magnetic field after the RF pulse is applied. Consequently, the frequencies of FID signals (f_{FID}) become dependent on the position as in Equation 1.2.

$$f_{\text{FID}}(x) = \gamma(B_0 + B_{\text{Grad}}(x)) \tag{1.2}$$

In conclusion, the frequency information can be mapped to the position one in MRI. Our project also adopts this idea to find the position of the catheter. The operating principle the project, which encompasses this thesis work, can be summarized as follows: There is a microsystem at the tip of the catheter, which transfers the frequency information to the outside of the MRI machine via optical methods. Firstly, the FID signal around the tip is received and down-converted by an optically powered CMOS module. Next, this CMOS module drives an RF MEMS module with the down-converted signal as an electrical current. After that, the RF MEMS module converts the electrical signal to a mechanical one and the latter is transmitted for further processing via an optical readout method. In this thesis work; design, fabrication, and characterization of RF MEMS resonators are done for these given tasks.

The actuation mechanism of MEMS resonators is based on the Lorentz force. When the current and the magnetic field are positioned as in Figure 1.1 [1], the force is induced in the out-of-plane direction. The main advantage of using this method is that it allows us to utilize the huge DC magnetic field in MRI machine, which is

1.5 T or 3 T for clinical-MRI, thereby resulting in a low-power solution. Even weak currents, on the order of 0.1 mA, can produce strong Lorentz force (39 nN for 130 μm-long bridge) under 3 T external field strength according to Equation 1.3, where F_L is the Lorentz force, i is the current, l_r is the length of the resonator, and B_0 is the external field strength.

$$F_L = il_r \times B_0 \tag{1.3}$$

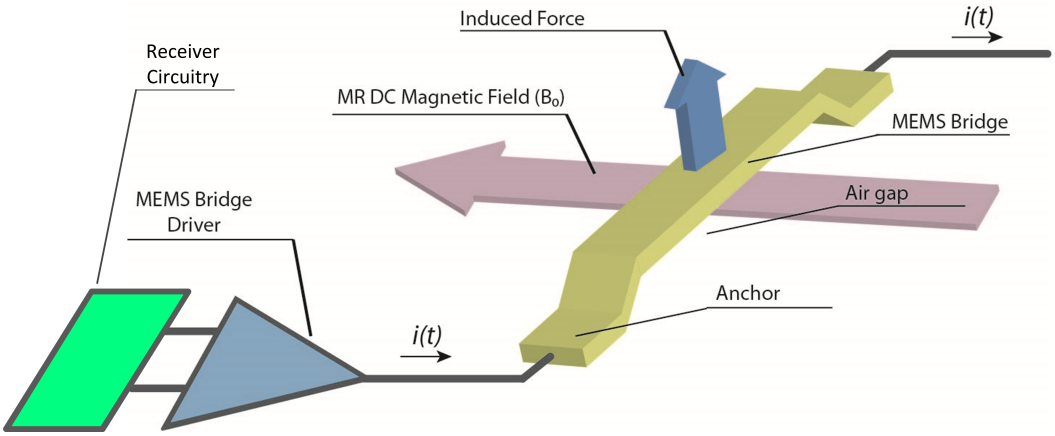

Figure 1.1. Actuation mechanism for MEMS resonators.

In summary, the most important contributions of this thesis work to the literature are the utilization of MRI device's external DC magnetic field for the actuation mechanism and the use of optical methods for detecting the mechanical signal produced by the resonator structures. As it is mentioned, the main advantage of the first one is decreasing the power consumption. In addition, the second one eliminates the use of metal wires, which is problematic in MRI environment.

In general, it is possible to divide designs into two main groups. The first group consists of micromirror resonators, whose deflection is read by optical means. In this work, the emphasis is on laser Doppler vibrometry (LDV) method. The second group is comprised of diffraction grating resonators. The optical readout method for this case is diffraction gratin interferometry (DGI). These groups will be investigated in detail

in two individual chapters. These chapters explain the design procedure in terms of theory, analytical calculations, device specifications and finite element analysis (FEA) simulations. Chapter 4 discusses how masks are designed and the fabrication process is conducted. Chapter 5 shows the characterization results for the fabricated devices. Finally, Chapter 6 concludes the thesis and comments about the possible future work.

2. DESIGN OF MICROMIRROR RESONATORS

Since LDV method can detect velocity of a mechanical structure in the direction of the reflected laser beam, our aim was to design resonators which have reflective surfaces that can move in the desired - in this case out of plane- direction. Although our different resonators have different geometry, the main idea is to have a clamped-clamped approach with a reflective mirror in between. Figure 2.1 shows an example of this type of resonators.

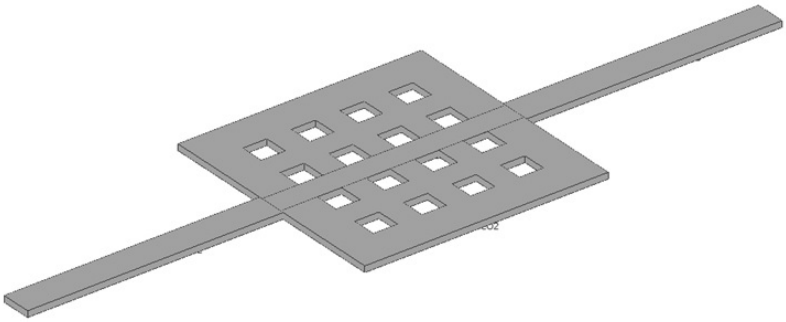

Figure 2.1. Clamped-clamped resonator with reflective mirror.

Note that the resonator has perforation holes in its mirror part. There are two reasons why we decided to put these holes. These are reducing the air damping effect and easing the removal of sacrificial photoresist layer under the structure, which will be explained in detail in Chapter 4.

According to the actuation mechanism explained in Chapter 1, these micromirror resonators are capable of generating out-of-plane movement given that there is current passing through the structure and there is DC magnetic field parallel to the mirror plane and perpendicular to the direction of current.

Since the mechanical signal produced by a resonator is strongest around the resonance peak and gets weaker as frequency is farther away from the peak, it is hard to detect a useful signal throughout the whole frequency range of interest using only

one resonator. Therefore we designed resonator families which have different resonators that are connected in series. Due to this series connection approach, all resonators are actuated by the driving signal at the same time. These resonators have different geometry, which leads to different resonance frequency values. These resonance peaks are distributed such that the produced mechanical signal never drops below a certain threshold. By using an LDV spot which is big enough to cover all the resonators, we plan to detect strong signal for the whole frequency range. An example of such a family can be seen in Figure 2.2.

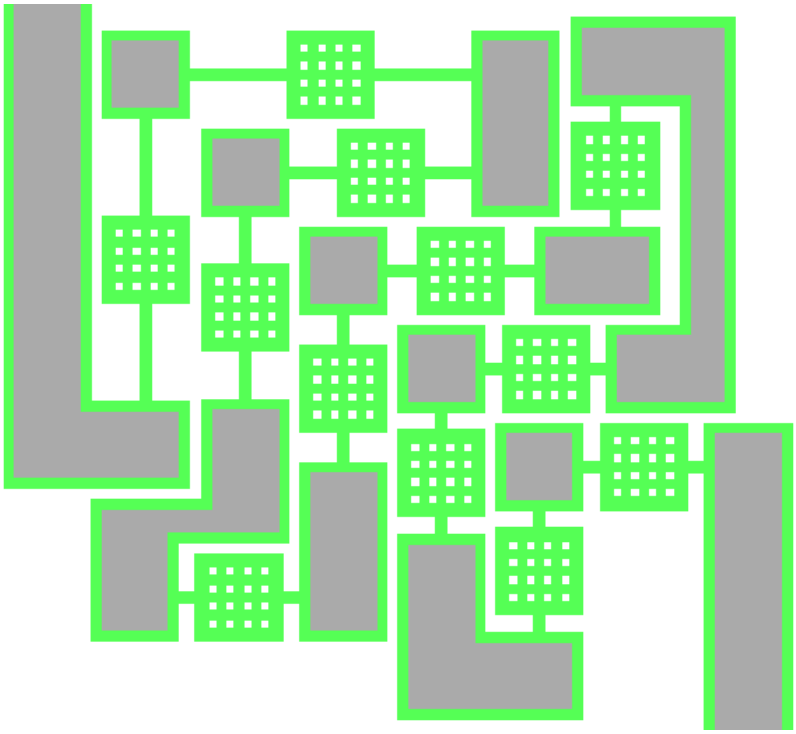

Figure 2.2. Series connected micromirror resonator family.

In the following subsections, we are going to investigate theoretical background, analytical calculations, properties of different families, and finite element analysis (FEA) simulations. We are going to finish the section with a conclusion.

2.1. Theoretical Background

In this section we are going to start with the mechanics of double-clamped beam with a central mass. After that we will continue with squeeze-film air damping.

2.1.1. Mechanics of Double-Clamped Beam with a Central Mass

In this discussion, our aim is to find the out-of-plane displacement function, $w(x)$, for a double-clamped beam with a central mass and the spring constant in the central part of the structure. Since the central mass is generally much wider and/or thicker than the supporting beams, we are going to assume that the beams have negligible mass compared to the central part and the latter one is doing a transversely translating motion without bending. The top view and the cross sectional view of the resonator structure along with the necessary dimensions, forces, and moments can be seen in Figure 2.3 and Figure 2.4, respectively.

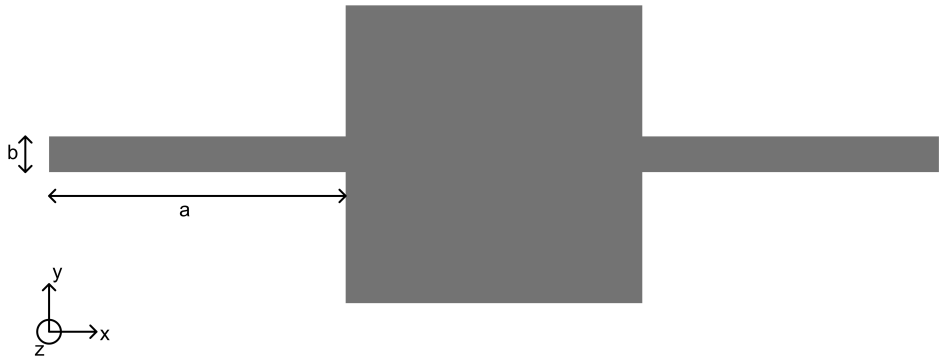

Figure 2.3. Top view of double-clamped beam with a central mass.

Figure 2.4. Cross-sectional view of double-clamped beam with a central mass.

We start with the general relation for bending moment of beam structures [32],

$$M(x) = -EIw'' \tag{2.1}$$

where E is Young's Modulus, I is moment of inertia of the beam, and w is the displacement function in the z-direction with respect to x. For a beam with a rectangular cross section of width b and thickness t, the moment of inertia is [32]

$$I = \frac{bt^3}{12} \tag{2.2}$$

If we write the bending moment with respect to an arbitrary point x on the left beam, we obtain

$$M(x) = -m_0 + xF_0 \tag{2.3}$$

where m_0 is the restrictive moment and xF_0 is the moment due to the supporting force. Since there are two clamped ends, the supporting force is equal to half of the weight of the central mass which is $M_t g/2$, where M_t is the total mass and g is the gravitational acceleration. Using Equations 2.1 and 2.3 we have

$$-\frac{Ebt^3}{12}w''(x) = -m_0 + \frac{xM_t g}{2} \tag{2.4}$$

The boundary conditions for this differential equation are $w(0) = 0$, $w'(0) = 0$, $w'(a) = 0$, and $w''(a/2) = 0$. Using $w''(a/2) = 0$ in Equation 2.4 we have

$$m_0 = \frac{M_t g a}{4} \tag{2.5}$$

$$-\frac{Ebt^3}{6M_t g}w''(x) = (x - \frac{a}{2}) \tag{2.6}$$

Integrating both sides with respect to x yields

$$-\frac{Ebt^3}{6M_tg}w'(x) = \frac{x^2}{2} - \frac{ax}{2} + C_1 \tag{2.7}$$

Using $w'(0) = 0$ we get

$$C_1 = 0 \tag{2.8}$$

$$-\frac{Ebt^3}{3M_tg}w'(x) = x^2 - ax \tag{2.9}$$

Integrating one more time with respect to x yields

$$-\frac{Ebt^3}{3M_tg}w(x) = \frac{x^3}{3} - \frac{ax^2}{2} + C_2 \tag{2.10}$$

Using $w(0) = 0$ we obtain the displacement function

$$C_2 = 0 \tag{2.11}$$

$$w(x) = x^2(\frac{3a}{2} - x)\frac{M_tg}{Ebt^3} \tag{2.12}$$

Note that this function is valid for x values, which are on the left beam. Figure 2.5 shows the tendency of this function depending on x. Since we assumed that the central mass moves without bending, the displacement of mass can be expressed as

$$w(a) = \frac{a^3M_tg}{2Ebt^3} \tag{2.13}$$

We can also relate a spring constant for the central mass for the forces that perpen-

dicular to the plane.

$$k = \frac{F}{x} \tag{2.14}$$

In this case the force is the weight of the mass. Therefore

$$k = \frac{2Ebt^3}{a^3} \tag{2.15}$$

Note that the spring constant would be the same if we started our discussion for an external force instead of just the weight of the mass.

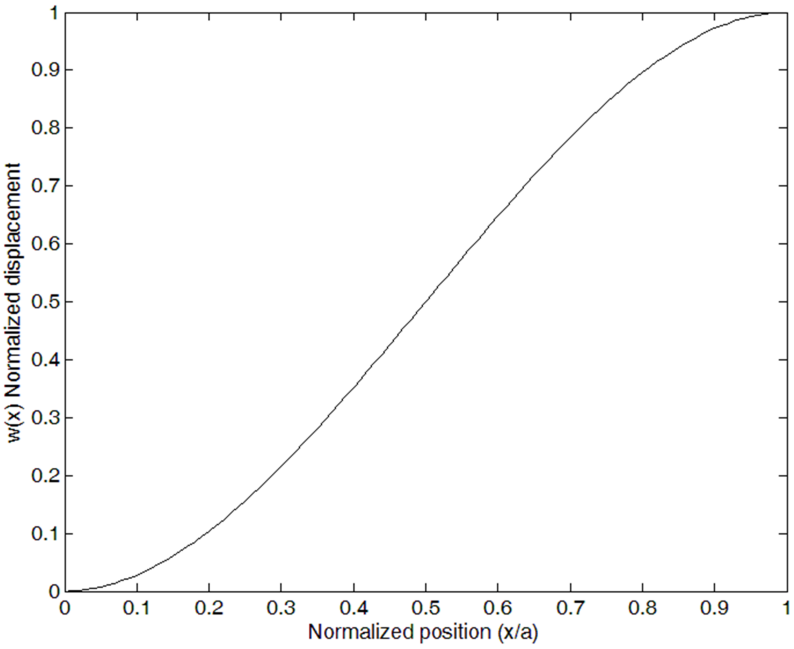

Figure 2.5. Tendency of $w(x)$ depending on x.

2.1.2. Squeeze Film Air Damping

As mechanical devices change in size, the forces acting on them also change, but the rate depends on the type of the force. Volume forces like gravity and inertia

are proportional to the cube of the scaling factor; on the other hand, surface forces like viscous force are multiplied by the square of it. Therefore, compared to the conventional machines, surface forces have much greater effect on MEMS devices as the size of the structures decreases. The surrounding air acts as an obstacle to the movement of the MEMS device and affects the dynamic behavior of it.

Structures moving in air already encounter with drag force damping, but things become more complicated as they get close to another surface, such as the substrate. Because of the squeeze film action of the air between these surfaces, there exists another damping mechanism and it can be stronger than the drag force of the air [33–36]. This mechanism is called squeeze film damping and it becomes more significant as the gap between the surfaces gets smaller and width of the device gets larger. Squeeze film damping is the dominant damping mechanism for MEMS devices which have large plates that move against a trapped thin air film. Consequently, it affects the dynamic behavior of the structure greatly.

The damping pressure between two plates has two components. The first one is due to the viscous flow of air when the movement of the structure pushes the air out of or sucks it into the gap and called the viscous damping force. The other component is the elastic damping force, which is caused by the compression of the air film. At low frequencies, the air film is not significantly compressed; therefore the viscous damping force dominates. The viscous damping force is proportional to the velocity of the plate. At high frequencies, the air fails to escape the gap, hence it is compressed. In this case the elastic damping force dominates. This force is proportional to the displacement of the plate. There is a frequency, at which the viscous damping force is equal to the elastic damping force. This frequency value is called the cut-off frequency (ω_c) of squeeze film damping.

The viscous damping force has a related damping coefficient c_d and the elastic damping force has a spring constant k_e associated with it. Both of these variables are functions of the vibration frequency. The governing equation for the dynamic behavior

of the vibration system can be written as

$$m\ddot{z} + c_d\dot{z} + (k_e + k_0)z = F_d \sin \omega t \tag{2.16}$$

where m is the mass, z is the displacement of mass in the z-direction (direction normal to the plane), k_0 is the spring constant of the mechanical structure, and F_d is the amplitude and ω is the angular frequency of the driving force. The solution to this differential equation is

$$z(\omega) = A_0 \sin(\omega t + \varphi) \tag{2.17}$$

where the amplitude A_0 is

$$A_0 = \frac{F_d}{m}\sqrt{\frac{1}{(\omega_a^2 - \omega^2)^2 + \frac{c_d^2\omega^2}{m^2}}} \tag{2.18}$$

and the phase difference φ is

$$\varphi = -\arctan\frac{c_d\omega}{m(\omega_a^2 - \omega^2)} \tag{2.19}$$

where

$$\omega_a^2 = \frac{(k_e + k_0)}{m} = \omega_0^2 + \frac{k_e}{m} \tag{2.20}$$

Since both k_e and c_d -consequently ω_a- are functions of ω, the dynamic behavior of the vibration system depends heavily on the ratio of the natural vibration frequency ω_0 and the cut-off frequency of squeeze film damping ω_c. Now we are going to investigate three different cases; where the ratio is much smaller than unity, close to unity, and much greater than unity.

If the cut-off frequency is much larger than the natural vibration frequency, the viscous damping constant c_d is almost constant and the elastic force is negligible.

The gas film is incompressible and the dynamic behavior is determined mostly by the damping ratio ζ. Figure 2.6 shows the underdamped, overdamped, and critically damped cases [37].

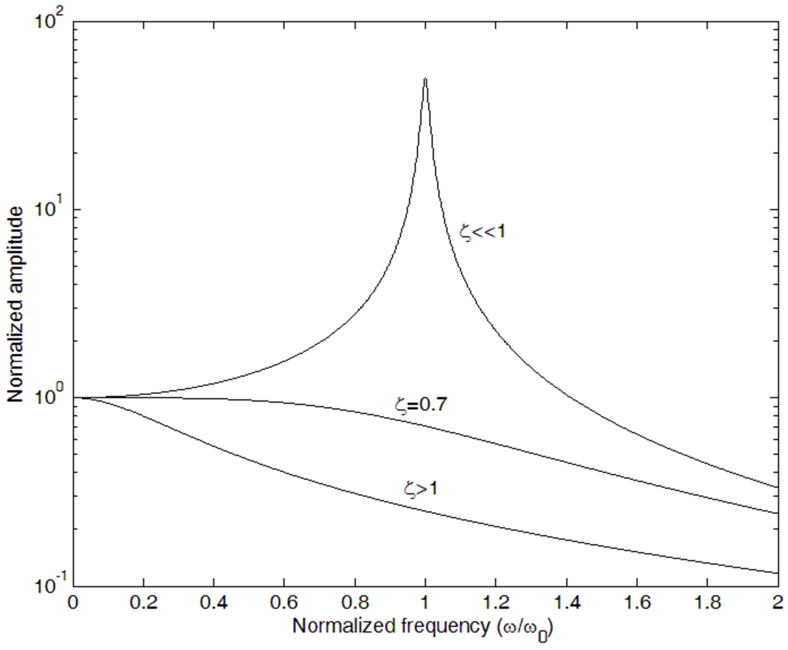

Figure 2.6. Dynamic behavior of the vibration system for $\omega_0 \ll \omega_c$.

When ω_0 is comparable to ω_c, the most interesting dynamic behavior occurs. Figure 2.7 shows the frequency response of the system [37].

Because of the strong damping effect at cut-off frequency, the amplitude declines as ω_c approaches ω. The ratio of k_e/k_0 determines the amount of the decline. Frequency and amplitude of the resonance peak depends on c_d. In this condition, both viscous and elastic components play important role on the dynamic behavior.

In the third and the final case, where $\omega_0 \gg \omega_c$, the spring constant of the structure is much greater than that of the elastic damping. The amplitude of the frequency response decreases as ω approaches ω_c, however the effect is not significant since k_e is relatively small. As seen in Figure 2.8, there is a resonant peak at a frequency which is slightly higher than the natural vibration frequency due to the elastic damping

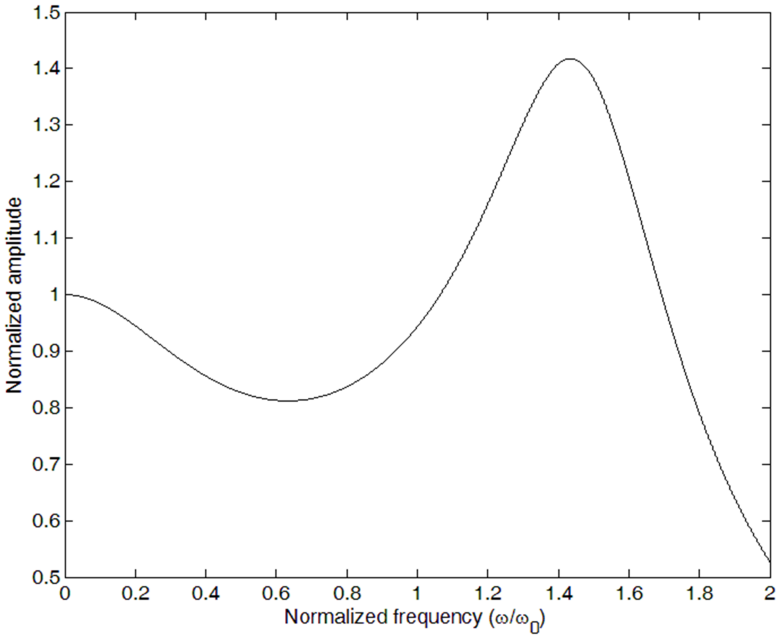

Figure 2.7. Dynamic behavior of the vibration system for $\omega_0 \approx \omega_c$.

force [37]. Since the viscous damping force is small at high frequencies, the resonant peak is generally high. As a result, when $\omega_0 \gg \omega_c$, the effect of both the elastic and the viscous damping is slight.

2.2. Analytical Calculations

Although FEA simulations are extremely useful for designing MEMS resonators, it is impossible to simulate every possibility, such as geometry and material differences. Therefore one needs to find a good starting point before going into simulations and analytical calculations are vital to find such a point.

For LDV compatible design, we had decided to have double-clamped beams with a reflective central mass that has perforation holes, as in Figure 2.1. According to the discussion in Section 2.1.1; for the resonator, whose top view is given in Figure 2.9, the spring constant for the central mass moving in the normal direction to the plane

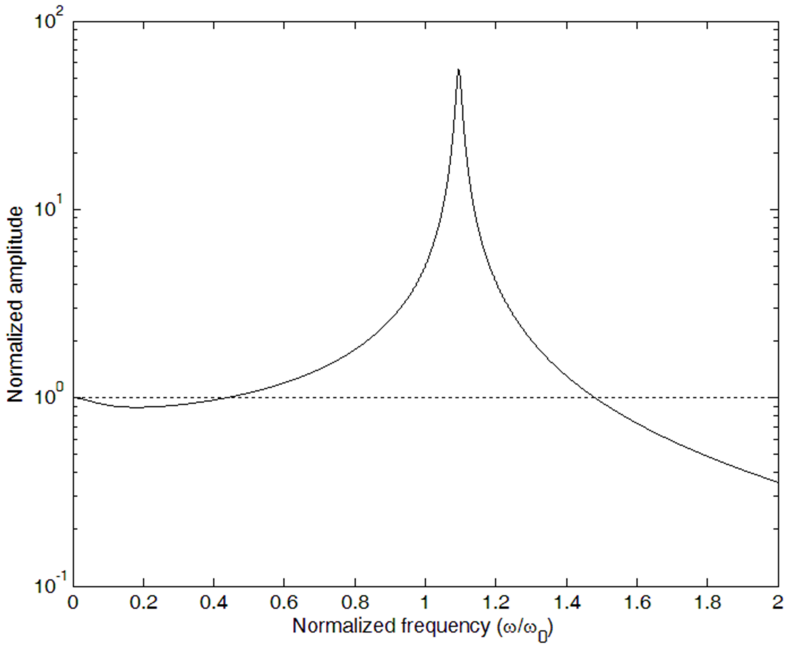

Figure 2.8. Dynamic behavior of the vibration system for $\omega_0 \gg \omega_c$.

can be found as

$$k = 2\frac{Ewt^3}{l^3} \tag{2.21}$$

where E is Young's modulus and t is the thickness of the structure, which is uniform everywhere. On the other hand, the mass of the central part is given by

$$m = (b^2 - 16a^2)t\rho \tag{2.22}$$

where ρ is the density of the material.

If we think about the structure as a spring-mass system, the resonant frequency is

$$f_{\text{res}} = \frac{1}{2\pi}\sqrt{\frac{k}{m}} \tag{2.23}$$

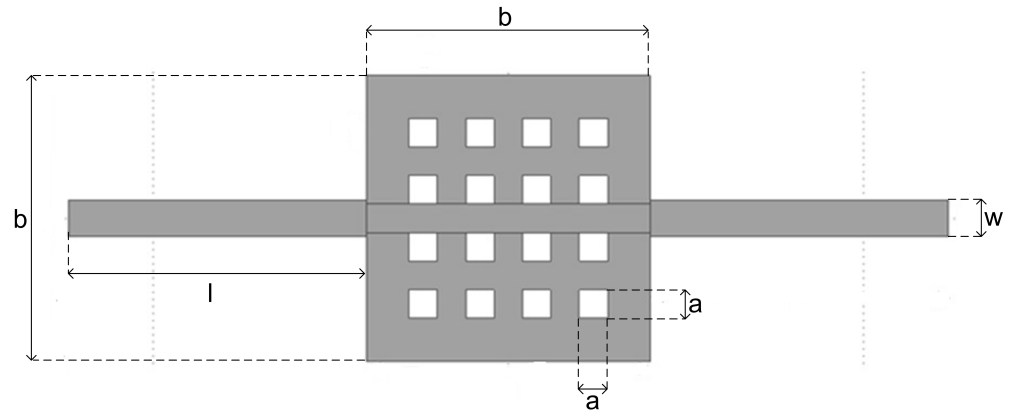

Figure 2.9. Top view of double-clamped beam resonator with a central mass.

$$f_{\text{res}} = \frac{1}{2\pi}\sqrt{\frac{2Ewt^2}{(b^2 - 16a^2)l^3\rho}} \tag{2.24}$$

For the LDV compatible case, we wanted to have family of resonators, which could cover the frequency interval of 1 kHz to 500 kHz. As a starting point, we wanted to construct a resonator, whose resonant frequency is 200 kHz. For the dimensions that are given in Figure 2.9, we chose b=40 μm, a=4 μm, t=1 μm, w=5 μm, and selected aluminum (E=70 GPa, ρ=2700 kg/m^3) as the structural material. Using Equation 2.24, we found that the length of one beam has to be 49.62 μm in order to assure that the resonant frequency is 200 kHz. Note that this calculation does not take squeeze film damping into account. After all, the intended use for this calculation is just to find an appropriate starting point for the simulations.

2.3. Resonator Families

In this section, we are going to introduce different designs which are intended for LDV optical readout method. We refer to every independently functional unit as a resonator family, due to the fact that every unit consists of at least three resonators which are connected in series. This number can go up to twelve in certain families.

There are many common things among the families. First of all, the operating principle that we explained in the beginning of Chapter 2 is the same for every family. They all utilize series connected, out-of-plane moving resonators, which are covered by a single LDV spot. Secondly, the structural material for all of them is aluminum. Finally, the central mass part of every resonator of every family has the same top-view geometry. As we mentioned before, the aim of having more than one resonator is to cover a broader frequency range. This requires different resonant frequency values for individual resonators in a certain family. Since the central mass is identical for all resonators, we achieved to adjust resonant frequency values by shifting the length of supporting beams of different resonators.

The reason why we have various resonator families is that they are optimized for different purposes. There are two important factors that we take into consideration while designing a family. These are film thickness and power consumption. Using the same mask set, it is possible to fabricate MEMS structures with different film thickness values, because film thickness is not determined by the layout but by the material deposition process. Since both thick and thin films have certain advantages and disadvantages, we decided to have optimum families for two different film thickness values, which are 0.5 μm and 1 μm.

The second factor is the power consumption of the structure. While we were designing the MEMS structures, the driving capability of the external circuit was unknown. Therefore, we decided to optimize devices for three different peak current values, which are 0.1 mA, 0.2 mA, and 0.5 mA. In most cases, resonators which belong to low-power families have narrower supporting beams, because they have smaller spring constant and easier to move. Having various designs for different peak current values is especially beneficial to avoid drawbacks of nonlinear behavior of the structures. It is possible that the resonant points for a certain family are shifted due to nonlinearity, when the driving force is significantly different.

Our actuation approach assumes that the DC magnetic field and the direction of current flow through the resonators are orthogonal to each other. However, this

assumption may not always hold. In order to avoid parallel alignment of the current and the magnetic field, we designed our families such that every resonator is used two times with 90 degrees orientation difference, as in Figure 2.2. The obvious disadvantage of this approach is that it results in too much area consumption. In order to have smaller resonator families in addition to these, we also designed the same families with non-repeating units. As it can be seen in Figure 2.10, the orientation is the same for all the resonators and the angular difference compared to the previous case is 45 degrees. The reason for this difference is that we assume the magnetic field is most of the time either horizontal or vertical with respect to the page. This orientation is capable of producing mechanical signal for either case.

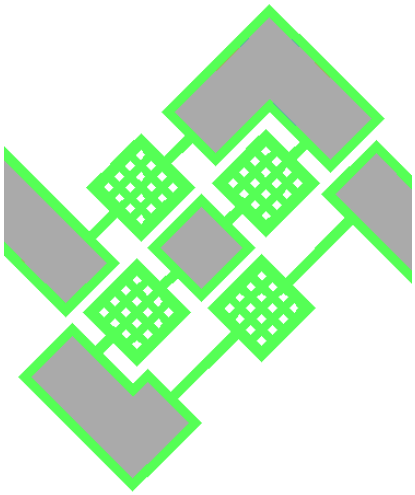

Figure 2.10. Micromirror resonator family with non-repeating units.

Along with the repeated-resonator option, we introduced another variation by splitting the supporting beams as in Figure 2.11. The aim of this variation is to make the undesired torsional motion harder and to prevent the structure from collapsing to one of its sides. The drawback of this variation is that it is more difficult to fabricate these split beams, which are supposed to have half the width of the non-split ones. Consequently, we only applied this variation to the widest beams which have 5 μm width.

All in all, we designed various resonator families which differ in terms of power

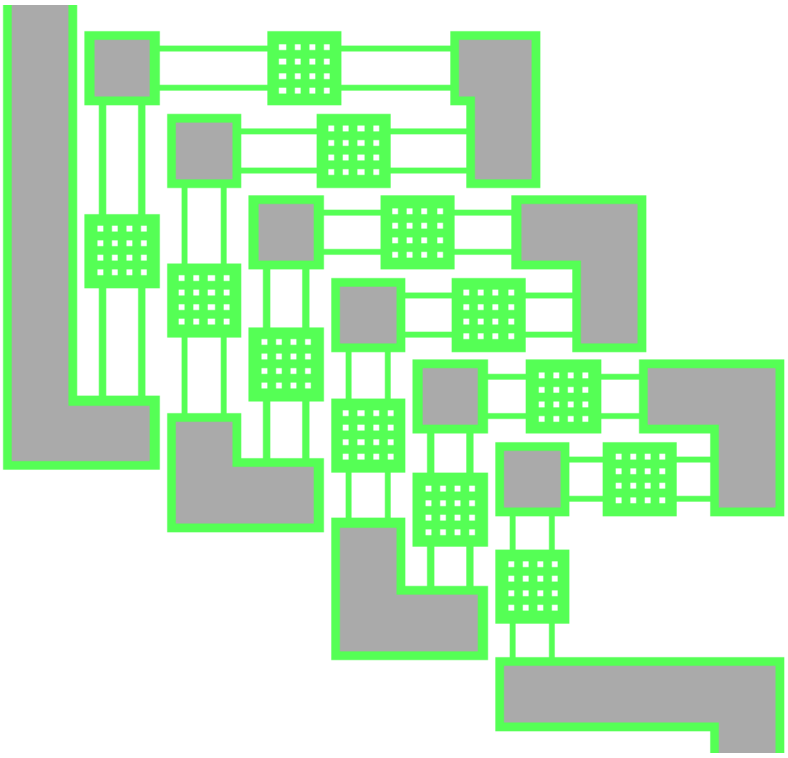

Figure 2.11. Micromirror resonator family with split supporting beams.

consumption and film thickness. In addition, there are two types of each resonator family, either with repeating or non-repeating units. Furthermore, for some of the families there is the split-beam option for both repeating and non-repeating types.

2.4. FEA Simulations

Although analytical calculations give us general idea about the behavior of structures, they have to be supported by more detailed simulations, because of many simplifications and assumptions. In order to have more reliable results, one needs to benefit from finite element analysis methods despite their time consuming and non-transparent nature.

COMSOL Multiphysics 3.5 MEMS Module's Solid, Stress-Strain with Film Damping application mode is used for FEA simulations. We can divide the these simulations into two categories, which are mode analysis and frequency response simulations. The

aim of the first one is to see if the movement pattern of the structures is appropriate for our optical readout methods. The goal of the frequency response simulations is to determine the strength of the mechanical signal depending on the frequency and power of the driving current. Now, we are going to discuss the results for both types in two individual subsections.

2.4.1. Mode Analysis Simulations

Although we designed many resonator structures with different geometry, these structures have similarities, such as the shape of the central mass. In order to make things simpler and clearer, we are going to show results for one sample structure, because the other ones behave in a similar manner. For this structure, the beam length is 60 μm, width is 5 μm, thickness 1 μm, the central mass is 3.63 ng, and the material is Al (E=70 GPa, ρ=2700 kg/m^3). The first four mode shapes can be seen in Figure 2.12. According to Equation 2.24, the out-of -plane mode for this structure is calculated to be at 150.4 kHz, whereas the simulation result gives the same mode at 120 kHz. The difference between these two stems from the assumption in the analytical calculation that the central mass does not bend, which is not entirely correct.

As it can be seen in Figure 2.12, the first structural mode is an out-of-plane motion of the central mass. This kind of movement is the most desirable type for LDV optical readout approach, which can detect vibration in the direction of the incident laser beam. Therefore we can conclude that our design is appropriate for our readout method as far as modal behavior is concerned.

2.4.2. Frequency Response Simulations

In Section 2.4.1, we discussed the structural mode analysis simulations, in order to verify that our resonators are capable of moving in the appropriate manner for LDV optical readout method. In this subsection, we will be discussing another type of FEA, which is called the frequency response simulations. One goal of these simulations is to determine an optimum thickness value for the air film under the resonators. The other

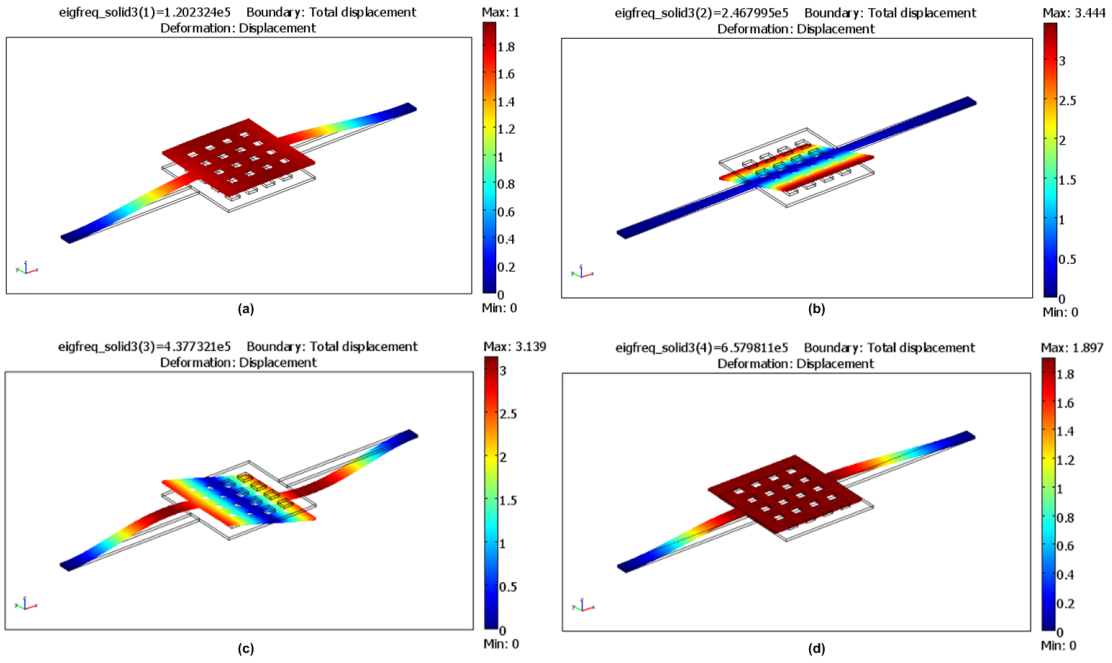

Figure 2.12. (a) The first structural mode (out-of-plane) for a single-beam resonator at 120 kHz. (b) The second structural mode (torsional) at 247 kHz. (c) The third structural mode (out-of-plane) at 438 kHz. (d) The fourth structural mode (in-plane) at 657 kHz.

and more important aim of these simulations is to determine the dynamic behavior of the mechanical structures. In other words, we want to obtain the dependence of the mechanical signal, which is produced by resonators, on the frequency and the amplitude of the driving force. In this case, the amplitude of the driving force depends on the strength of both the driving current and the external magnetic field. Since the magnetic field is not time varying, the frequency of the force depends only on that of the driving current.

In this subsection we will be discussing five subjects related to the frequency response simulations. Firstly, we will be explaining how we handled the border effect phenomenon for squeeze film air damping. Secondly, we will mention how we determined an appropriate tangential momentum accommodation coefficient (TMAC) for the simulations. Next, we will find the optimum air film thickness by utilizing simulation results. After that, we are going to discuss the relationship between the driving current and the mechanical signal amplitudes in detail. In the end, we are going to show the final results for different resonator families.

2.4.2.1. Border Effect for Squeeze Film Air Damping. For squeeze film damping simulations, the trivial way of finding a solution is to assume that the pressure change (Δp) which is caused by the movement of the structure is zero at the boundaries of the gas film. This assumption is beneficial for the cases where the device dimensions are much larger than the film thickness. However, for the devices which do not have high aspect ratio, it leads to inaccurate results. Vemuri *et al.* [38] showed that border effect is significant for the cases where the width/thickness ratio is even as high as 20. In order to include the damping effect at the boundaries, one should determine a relative elongation coefficient to calculate a new effective width for the structure as in Equation 2.25.

$$w_{\text{eff}} = \Delta L_r w \tag{2.25}$$

where w is the width of the structure, w_{eff} is the effective width, and ΔL_r is the relative elongation. The effective width is defined such that the trivial solution to the problem for that value gives an equivalent result for the real case.

In our case, we needed to take border effect into consideration because the size of the air gap was comparable with the width of our beam structures. In order to find relative elongation values, we used the data given in Table 2.1 [39] and interpolated from them as necessary.

Table 2.1. Relative elongation for different aspect ratios.

Aspect Ratio	**Relative Elongation**
4	0.8275
8	0.7270
16	0.6805
32	0.6559

2.4.2.2. Tangential Momentum Accommodation Coefficient. One of the parameters, which is needed for the squeeze film damping simulations is tangential momentum accommodation coefficient (TMAC). For monatomic gases, TMAC is around 0.93 and it does not depend on Knudsen number. On the other hand, TMAC for air depends on many things, including Knudsen number, surface cleanness and roughness, and temperature. Unfortunately, it is not easy to find a precise value for TMAC in our case; however, we can be confident that 0.85-1.00 interval includes it [40]. Therefore, we decided to run simulations for different TMAC values in this interval.

We conducted frequency response simulations for the double-clamped beam structure in Figure 2.13. For this device, the beam length is 102 μm, width is 3 μm, thickness is 1 μm, and the material is aluminum. The air film thickness is defined as 2 μm. Finally, the peak current is 1 mA and the magnetic field strength is 3 T.

The peak displacement and the quality factor results are given in Table 2.2.

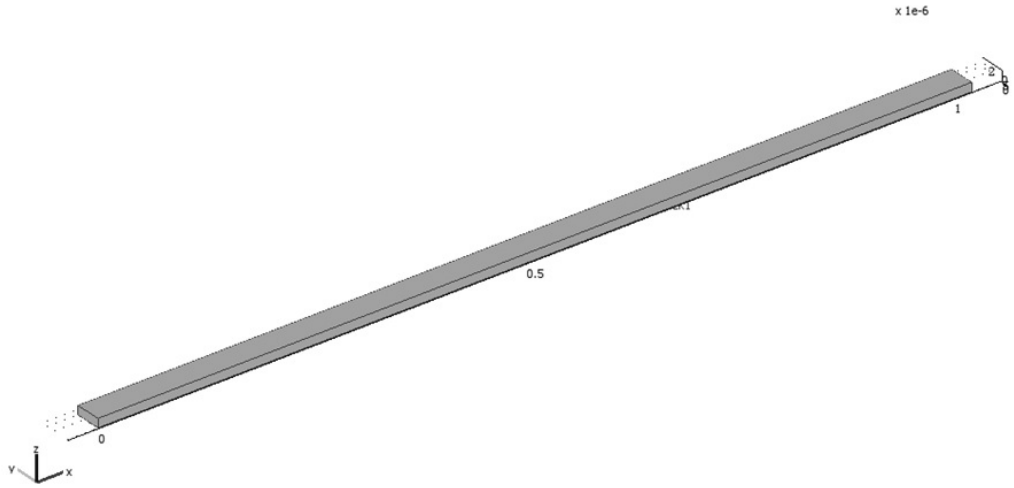

Figure 2.13. Double-clamped beam.

We can conclude that the difference among results, which is at most 4%, is quite acceptable. After that point, we decided to continue with the worst-case TMAC value of 1 for the following simulations.

Table 2.2. The effect of TMAC on dynamic behavior.

TMAC	**Peak Displacement (m)**	**Q Factor**
1.00	4.8e-6	97.5
0.95	4.8e-6	97.5
0.90	4.9e-6	99
0.85	5.0e-6	101

2.4.2.3. Determining the Optimum Film Thickness. As we mentioned before, determining an optimum value for air film thickness is one of the two main goals that we have. We know that the thinner the gas film gets, the more significant the squeeze film damping becomes. On the other hand, the air gap cannot be much thicker than the structure itself; otherwise the anchors become unreliable. Therefore we need to set a thickness, which is thin enough to result in good anchors, and at the same time, thick enough to cause reasonable damping.

In order to solve this problem, we adopted an approach similar to the TMAC case. We used the same structure, driving current, and magnetic field as we did for simulating the effect of different TMAC values. We repeated the simulation by changing only the air film thickness parameter. The results can be seen in Table 2.4.

Table 2.3. The effect of air film thickness on dynamic behavior.

Film Thickness (μm)	**Disp. amp. at resonance (m)**	**Q Factor**
0.5	3.66e-7	7.51
1.0	1.37e-6	28.27
2.0	4.83e-6	101.30

It is obvious that the film damping effect is much less for the thickness of 2 μm. This value is also comparable with the intended structural thickness range, which is from 0.5 μm to 2 μm, thereby resulting in strong anchors. In all of the following simulations, the film thickness will be set to 2 μm.

2.4.2.4. Current vs. Velocity. After determining the optimum air film thickness, we started to run frequency response simulations with double-clamped beam resonators which have perforated central mass structures as in Figure 2.1. The results show that the dynamic behaviors of the structures are not entirely linear. In other words, when we double the amplitude of the driving force at a certain frequency, which is proportional to the current amplitude at that frequency; the mechanical output, such as velocity, does not simply double. This nonlinear behavior is very hard to predict using analytical calculations and acts differently for various beam lengths. Therefore, we simulated certain structures for various driving current values. The results are given in Table 1.4.2.4.

In these simulations we used three resonators, which only differ in terms of the length of their supporting beams. The beam length stands for the length of one of the supporting beams on either side of the structures. We simulated all three resonators

Table 2.4. Normalized velocity at resonance vs. driving current.

Current Amp. (mA)	**17 μm beam**	**20 μm beam**	**58 μm beam**
0.1	1	1	1
0.2	0.73	1.92	1.05
0.5	0.57	2.47	1.08
1.0	0.52	2.67	1.09
2.0	0.49	2.72	1.10

for five different current values. The magnetic field strength was taken as 3 T in all cases. In addition beam widths were 5 μm and metal thicknesses were 1 μm. In Table 2.4, velocity values are normalized with respect to the ones which are expected for the corresponding current value. For example, the value 1.92 which corresponds to 0.2 mA current for 20 um long beam means that the velocity for 0.2 mA is 3.84 times greater than that of 0.1 mA since it is already expected to be 2 times larger.

One reason for this kind of a nonlinear result can be related to the nonlinear and frequency dependent behavior of film damping. Because of the latter one, the effect is different for devices which have different resonant frequency values.

As the reader can recall from Section 2.3, we designed resonator families which are optimized for a certain driving current value. The most important reason why we needed to do it that way is the complex relation between the driving current and the mechanical signal.

2.4.2.5. FEA Results for Resonator Families. In Section 2.3, we explained the important factors for designing resonator families, how they differ from one another, and what the variations are in a certain family. Now we are going to provide results of frequency response simulations for every resonator in all six families.

Firstly, Family 1 is optimized for 0.1 mA AC current amplitude. It has six

resonators, whose beam lengths are 17 μm, 22 μm, 26 μm, 31 μm, 41 μm, and 60 μm. It has metal film thickness of 1 μm and beam width of 3 μm. It produces above 30 mm/s velocity amplitude for the frequencies greater than 82 kHz. Its output drops to 2 mm/s at 13 kHz. The results for each beam can be seen in Figure 2.14.

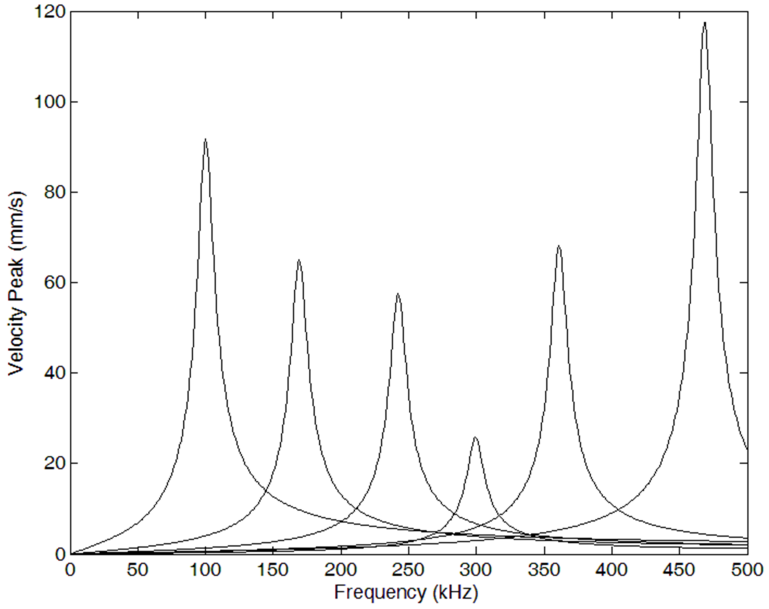

Figure 2.14. The frequency response of Family 1.

Family 2 is optimized for a higher input power value. The current amplitude for this family is 0.2 mA. It has only three different resonators, which is the smallest number among all families. Its beams are 4 μm wide and 1 μm thick. They are 20 μm, 32 μm, and 60 μm long. Above 80 kHz the output velocity amplitude is at least 40 mm/s and it drops to 2 mm/s at 7 kHz. The results can be seen in Figure 2.15.

Family 3 is again optimized for 0.2 mA, however it has five resonators, whose beams are 18 μm, 23 μm, 30 μm, 40 μm, and 60 μm long. Their width and the thickness are the same with the Family 2. It can produce at least 76 mm/s mechanical signal above 94 kHz. Its output decreases to 2 mm/s at 5 kHz. Figure 2.16 shows the dynamic behavior.

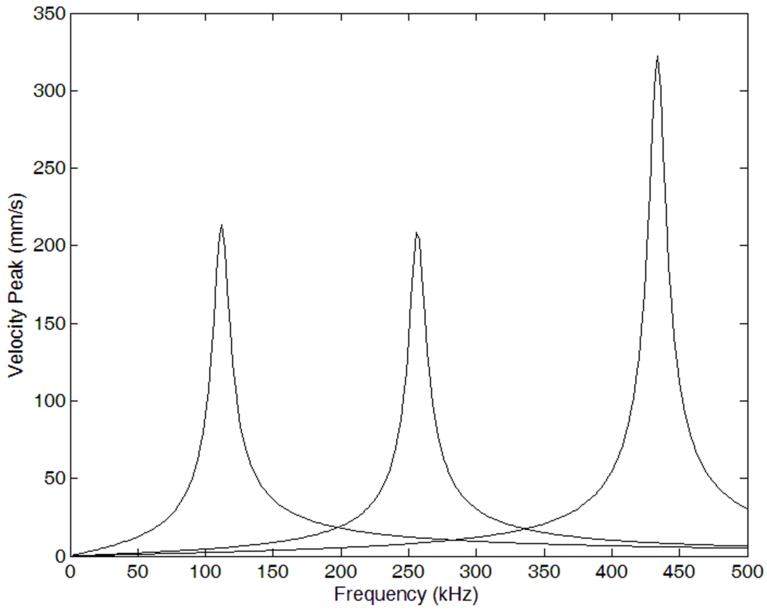

Figure 2.15. The frequency response of Family 2.

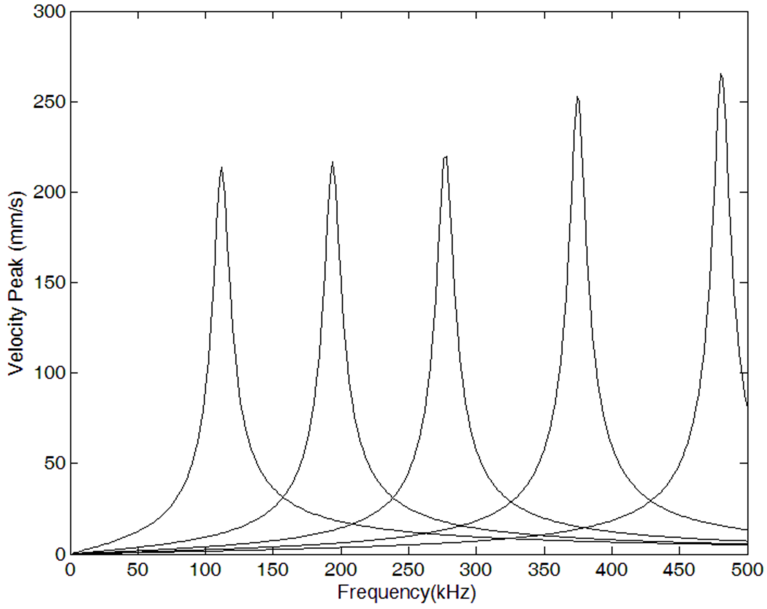

Figure 2.16. The frequency response of Family 3.

Family 4 is optimized for 0.5 mA current amplitude with six resonators whose width is 5 μm, and thickness is 1 μm. The lengths of the beams are 19 μm, 22 μm, 26 μm, 32 μm, 42 μm, and 60 μm. It produces higher output from the previous ones, which is above 171 mm/s above 102 kHz and drops to 2 mm/s at 3 kHz. The dynamic behavior for every beam can be seen in Figure 2.17.

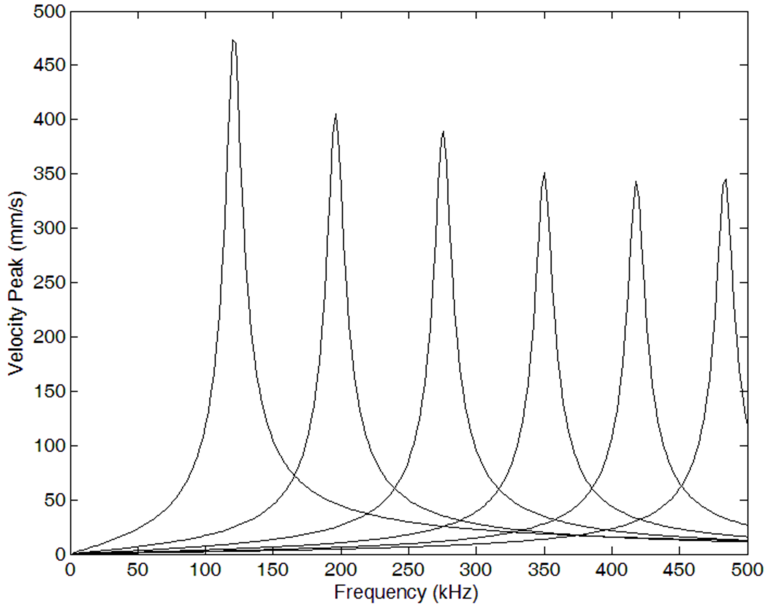

Figure 2.17. The frequency response of Family 4.

Family 5 is again optimized for 0.5 mA current amplitude but with four beams, whose width is 5 μm and thickness is 0.5 μm. It has two resonators, which have 8 μm-long beams. It also has two more resonators, whose beams are 16 μm and 45 μm long. Its output is above 101 mm/s above 53 kHz and higher than 2 mm/s even at 1 kHz. The results can be seen in Figure 2.18.

Family 6 is similar to Family 5 in terms of beam width, thickness, and peak current value. However it consists of three resonators, which have 8 μm-long beams and three other resonators, whose beams are 14 μm, 22 μm, and 45 μm in length. The mechanical signal is above 167 mm/s for frequencies higher than 65 kHz. The

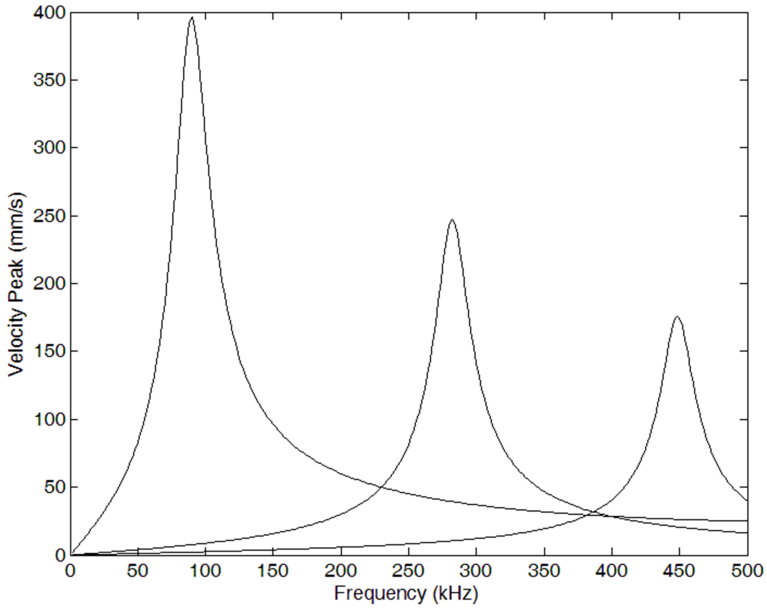

Figure 2.18. The frequency response of Family 5.

frequency for which it drops to 2 mm/s is the same with the previous case. Figure 2.19 shows the frequency response results.

The results for all families show that the mechanical signals they produce are strong enough to be detected by LDV technique. We specified where the velocity peak drops to 2 mm/s as a threshold; nevertheless, this is still much higher than the smallest signal which can be detected by an LDV system, which is on the order of 0.01 mm/s. We discuss these kinds of limits more thoroughly in Chapter 5.

An analytical transfer function that gives the relation between the driving force and the velocity can be derived from the Equation 2.26 for the vibration system

$$m\ddot{z} + c\dot{z} + kz = f_{dr}(t) \tag{2.26}$$

where m is the mass, c is the coefficient of damping force, k is the spring constant, z

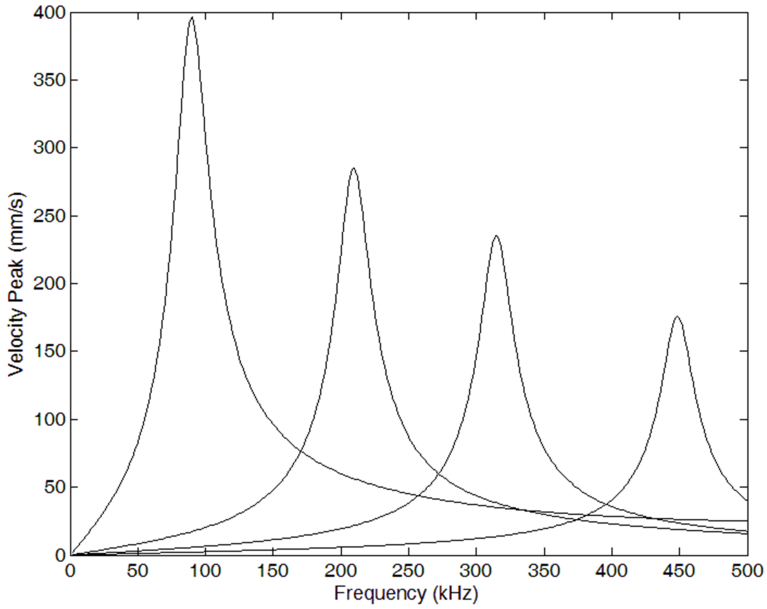

Figure 2.19. The frequency response of Family 6.

is the position, and f_{dr} is the driving force. Equation 2.26 can be written as

$$m\dot{v} + cv + k\int vdt = f_{dr}(t) \tag{2.27}$$

Taking the Laplace transform yields

$$msV(s) + cV(s) + \frac{k}{s}V(s) = F_{dr}(s) \tag{2.28}$$

The transfer function $H(s)$ becomes

$$H(s) = \frac{V(s)}{F_{dr}(s)} = \frac{s}{ms^2 + cs + k} \tag{2.29}$$

Transferring to Fourier domain by substituting $s = j\omega$ results in

$$H(j\omega) = \frac{j\omega}{j\omega c + k - m\omega^2} \tag{2.30}$$

Magnitude of the transfer function is

$$|H(j\omega)| = \frac{\omega}{\sqrt{c^2\omega^2 + (k - m\omega^2)^2}} \tag{2.31}$$

Substituting $\omega_0 = \sqrt{\frac{k}{m}}$ and $n = \frac{c}{2m}$ yields

$$|H(j\omega)| = \frac{\omega}{m\sqrt{(\omega_0^2 - \omega^2)^2 + 4n^2\omega^2}} \tag{2.32}$$

where n is the coefficient of damping and ω_0 is the free vibration frequency. Note that this transfer function has a bandpass characteristic, which is consistent with the simulation results.

3. DESIGN OF DIFFRACTION GRATING RESONATORS

In Chapter 2, we explained LDV compatible resonator structures, which form one of the two main divisions of our design. In this chapter, we are going to be discussing the second main division, which is comprised of diffraction grating interferometry compatible resonator structures.

We will begin the section with the necessary theoretical background about diffraction grating interferometry. Next, we will introduce our general approach and mention about main points which are valid for every designed structure. Then, we will continue with types and associated FEA simulations for these. Finally, we will explain some minor varieties in the layout.

3.1. Theoretical Background

The goal of diffraction grating interferometry method is to determine the displacement of a certain structure. In our case, we are interested in the displacement of our MEMS resonators. Figure 3.1 shows the schematic view for a diffraction grating interferometry setup.

In this approach, when the diffraction grating is illuminated by the light source, the reflected field splits into odd diffraction orders ($\ldots$, I_{-3}, I_{-1}, I_{+1}, I_{+3}, $\ldots$) in addition to the specular reflection (I_0) [41, 42]. The intensities of these diffraction orders depend on the interference of lights which travel two different paths. In the first path, the incident light reflects directly from the diffraction grating; whereas in the second one, it passes through the grating and reflects back from the surface underneath. Since these two paths do not have the same length, the light which travels either one has a different phase value. The intensities of the zero order and the

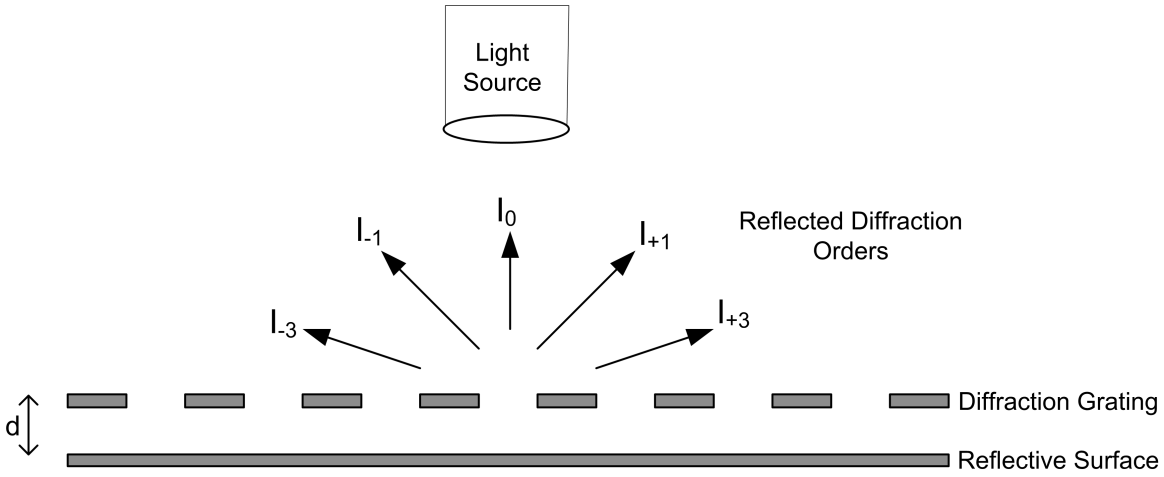

Figure 3.1. Cross section view of a phase sensitive reflective diffraction grating structure.

first orders can be given as in Equations 3.1 and 3.2

$$I_0 = I_{in} \cos^2\left(\frac{2\pi d}{\lambda}\right) \tag{3.1}$$

$$I_{\pm 1} = \frac{4I_{in}}{\pi^2} \sin^2\left(\frac{2\pi d}{\lambda}\right) \tag{3.2}$$

where I_{in} is the incident light intensity, d is the gap distance, and λ is the wavelength of the incident light. This discussion is valid if the light source is coherent with at least $2d$ of temporal coherence length [43].

If we assume that the reflective surface is fixed and the diffraction grating is free to move, we can use both $I_{\pm 1}$ and I_0 to determine the displacement of the grating structure. In order to have the maximum sensitivity and linearity for any reflected order, the measurement should be taken around a point d which is an odd multiple of $\lambda/8$, where the slope is maximum and the second derivative of the expressions with respect to the gap distance vanishes. This maximum sensitivity can be achieved even for large gap distance values, as long as it is an odd multiple of $\lambda/8$. Figure 3.2 shows

the normalized intensity with respect to normalized gap distance for reflected orders.

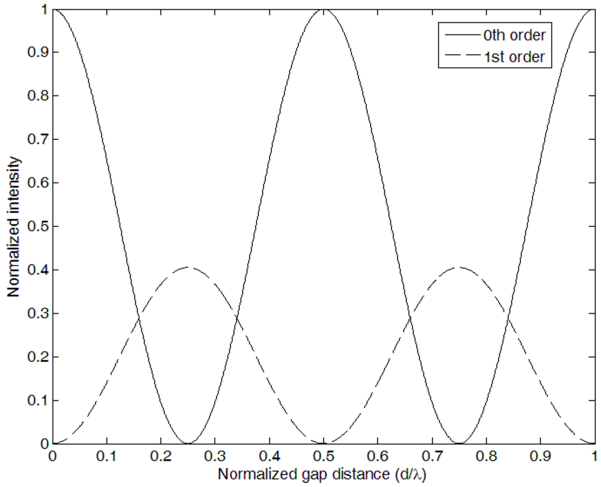

Figure 3.2. Normalized intensity vs. normalized gap distance.

One way of measuring a small displacement value Δx around an optimum point is to use two photodetectors for the zeroth and the first orders and computing the difference of the small signal outputs. The resulting current can be expressed as

$$i = R|\frac{\partial(I_0 - \alpha I_1)}{\partial d}\Delta x|_{d=\frac{\lambda}{8}} = RI_{in}\frac{4\pi}{\lambda}\Delta x \tag{3.3}$$

where R is the photodetector responsivity and α is the equalizing gain. This method yields the displacement sensitivity of a Michelson-type optical interferometer. The advantages of this scheme are increased signal level, efficient use of laser power, and reduction in the laser intensity noise [44]. Note that Equation 3.3 is valid for small displacement values. Larger displacement results in decreased linearity.

3.2. General Approach

Our design approach for the diffraction grating interferometry compatible MEMS resonators is quite similar to the one we adopted for the LDV compatible case. As in Figure 3.3, we used double-clamped resonator structures with a central mass. Actuation mechanism is the same for both cases; however we do not have series connected

resonators for this one. Instead of that, the whole frequency spectrum is covered by a single resonator. Since we use the same actuation mechanism, we are again interested in the out-of-plane displacement of the central mass.

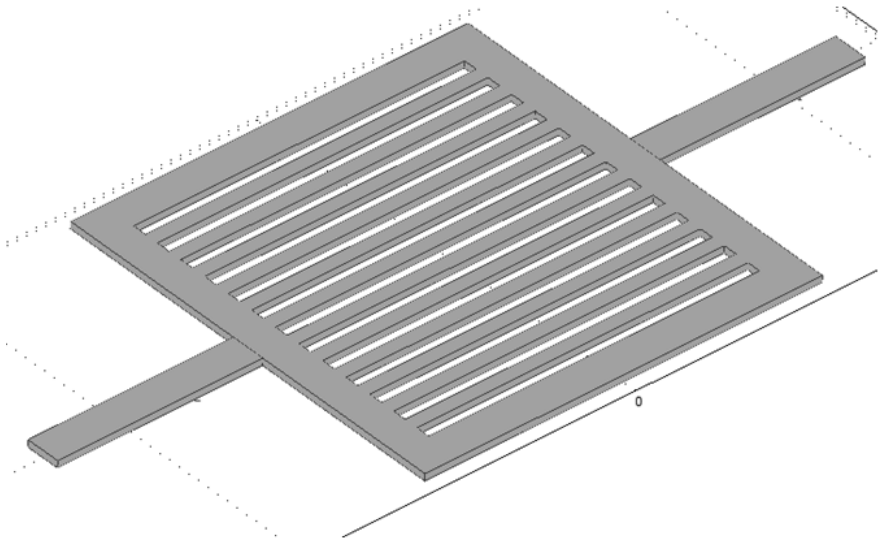

Figure 3.3. Diffraction grating resonator structure.

As we discussed in Section 3.1, diffraction grating interferometry method requires two reflective surfaces, one of which is in diffraction grating form. In our design, the released central mass of the MEMS resonator acts as the diffraction grating and the second reflective mirror is formed on the substrate. Figure 3.4 and 3.5 show a layout and a cross sectional view for this general approach, respectively.

3.3. Resonator Types and FEA Simulations

The main difference among our diffraction grating resonators is the period of diffractive elements. Here we define one period as the distance from the middle point of one ribbon to the same point of an adjacent one. We designed three different resonators, whose periods are 4 μm, 5 μm, and 6 μm. In this subsection, we are going to investigate each of these resonator structures in detail.

Firstly, we are going to start with the structural mode analysis of the resonator

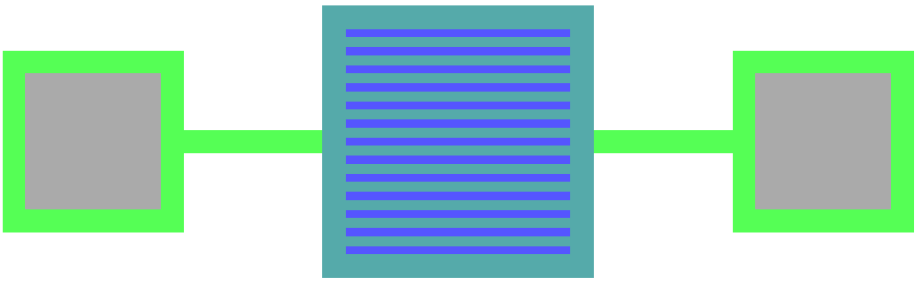

Figure 3.4. Layout of a diffraction grating resonator. Green color represents the released structure and dark blue represents the reflective mirror on the substrate. Light blue is for the overlapping areas for dark blue and green. Finally grey areas are anchor points.

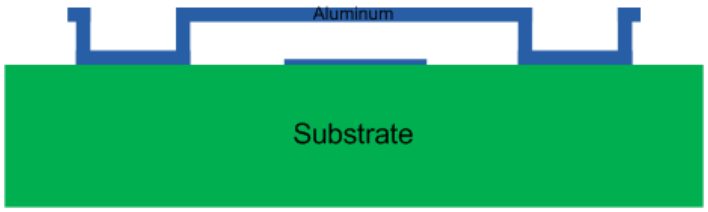

Figure 3.5. Cross sectional view of a diffraction grating resonator.

with 4 μm grating period. Structural mode analysis is especially important to see if there exists an out-of-plane mode shape which is convenient for our optical readout method. Figure 3.6 shows the related result for the resonator with 4 μm grating period.

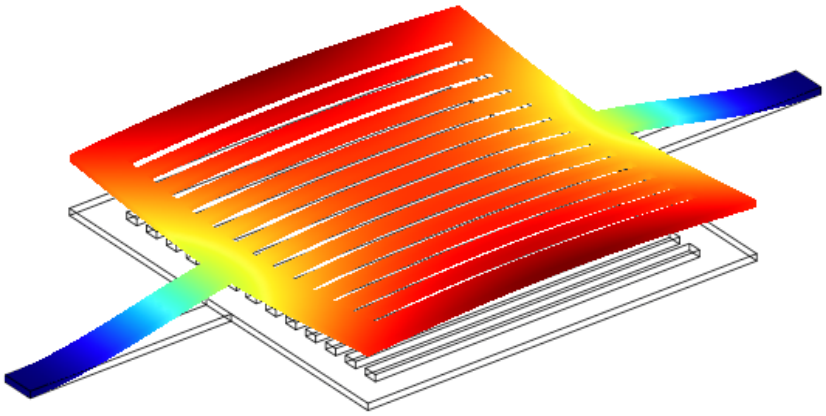

Figure 3.6. Out-of-plane structural mode for diffraction grating resonator at 190.12 kHz.

For this resonator, structural material is aluminum and its thickness is 1 μm. The other geometric parameters can be seen in Figure 3.7.

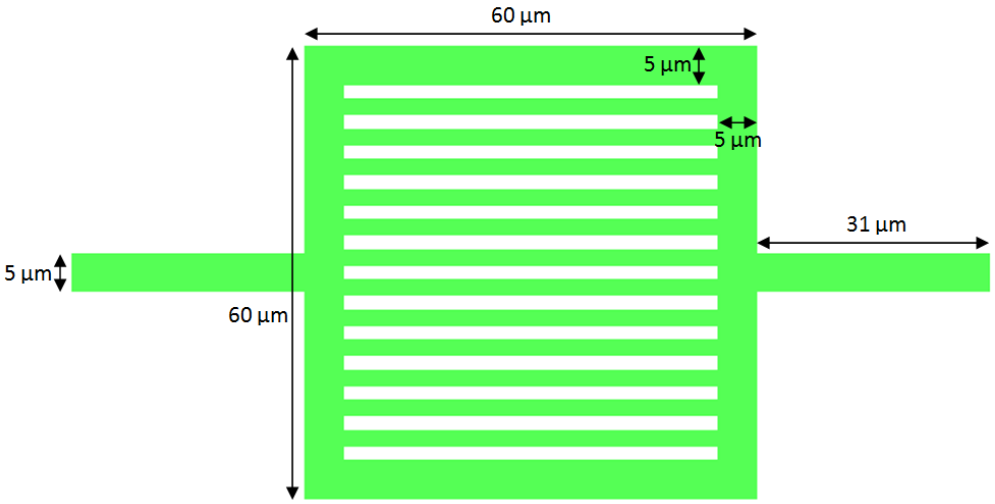

Figure 3.7. Top view of diffraction grating resonator with 4 μm grating period.

In order to find the optimum diffraction grating structure for a certain grating period value, we simulated devices for different supporting beam lengths, while keeping

the other parameters constant. Table 3.1 shows results for various structures. The simulations are done for 3 T magnetic field strength and 1 mA peak AC current. In this case the figure of merit is the value smallest displacement actuated by the resonator in 1 kHz to 500 kHz frequency range.

Table 3.1. FEA simulation results for resonators with 4 μm grating period.

Beam Length (μm)	**Disp. @1kHz (nm)**	**Disp. @500kHz (nm)**
10	4.6	1.5
20	11	0.2
25	18	0.8
29	21	0.6
30	25	2.4
31	26	3.3
32	30	2.7
33	34	1.9
34	35	0.7
35	38	0.6
40	54	0.4

Note that beam length of 31 μm gives the highest minimum displacement amplitude value. The whole frequency response curve for this device can be seen in Figure 3.8. The associated quality factor is 23.75.

For the resonators with 5 μm and 6 μm grating periods, we used the same approach in order to find the optimal supporting beam length. Table 3.2 shows FEA simulation results for resonators with 5 μm grating period. The magnetic field and the current values are the same as the previous case.

The best resonator has again 31 μm beam length, whose smallest displacement amplitude value is 6.2 nm which occurs at 500 kHz. The detailed frequency response curve can be seen in Figure 3.9. The quality factor for this case is 25.5.

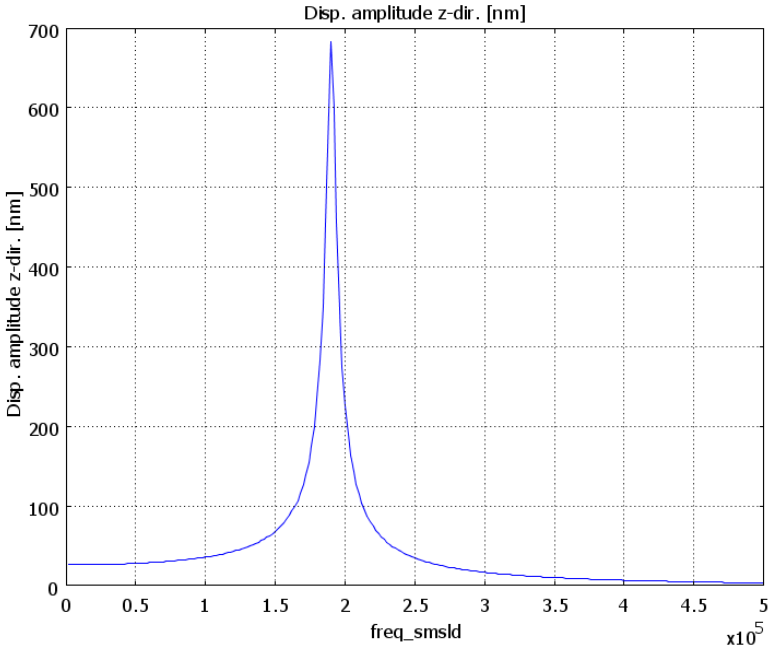

Figure 3.8. Frequency response of the resonator with 4 μm grating period and 31 μm supporting beam length.

Table 3.2. FEA simulation results for resonators with 5 μm grating period.

Beam Length (μm)	**Disp. @1kHz (nm)**	**Disp. @500kHz (nm)**
20	11	5.5
25	17	5.1
29	24	5.2
30	25	5.9
31	26	6.2
32	30	5.4
33	33	4.7
35	38	4.6
40	53	4.5

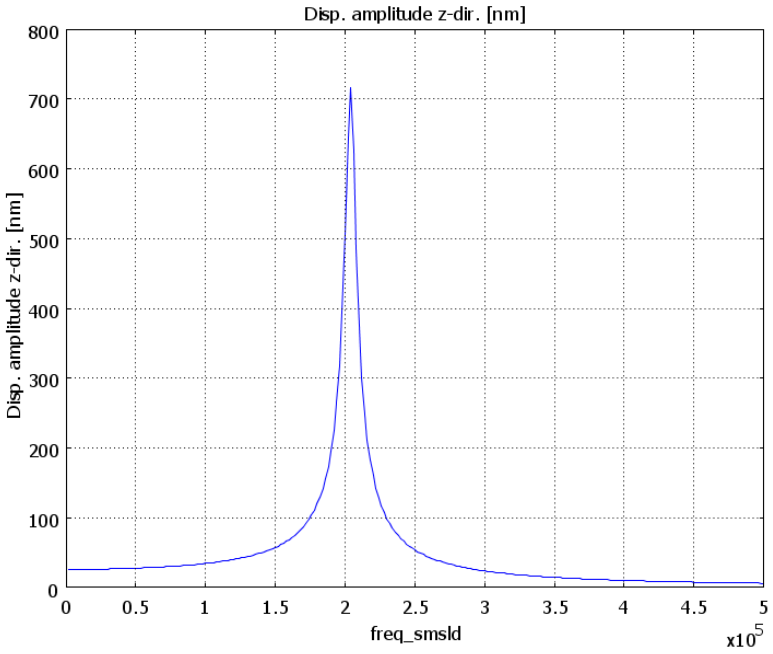

Figure 3.9. Frequency response of the resonator with 5 μm grating period and 31 μm supporting beam length.

Finally, we simulated the resonators with 6 μm grating period; again using 3 T magnetic field strength and 1 mA peak AC current. The simulation results for various resonators can be seen in Table 3.3.

The highest minimum displacement occurs for 30 μm beam length with 4.5 nm peak displacement at 500 kHz. Figure 3.10 shows the frequency response for this particular resonator which has quality factor of 22.89.

Among these three resonators that we designed, the worst one in terms of the minimum displacement value is the last one with 4.5 nm at 500 kHz. It is reported that the noise level for diffraction grating interferometry method can be as low as 20 $fm/\sqrt{Hz}$ in the DC to 2 MHz range [43]. Since we are interested in frequency values up to 500 kHz, the minimum detectible displacement level associated with that

Table 3.3. FEA simulation results for resonators with 6 μm grating period.

Beam Length (μm)	**Disp. @1kHz (nm)**	**Disp. @500kHz (nm)**
20	11.5	2.8
25	17.2	3.5
29	23.9	3.2
30	24.5	4.5
31	26.1	4.3
32	29.9	3.5
35	38.2	2.9
40	53.3	2.8

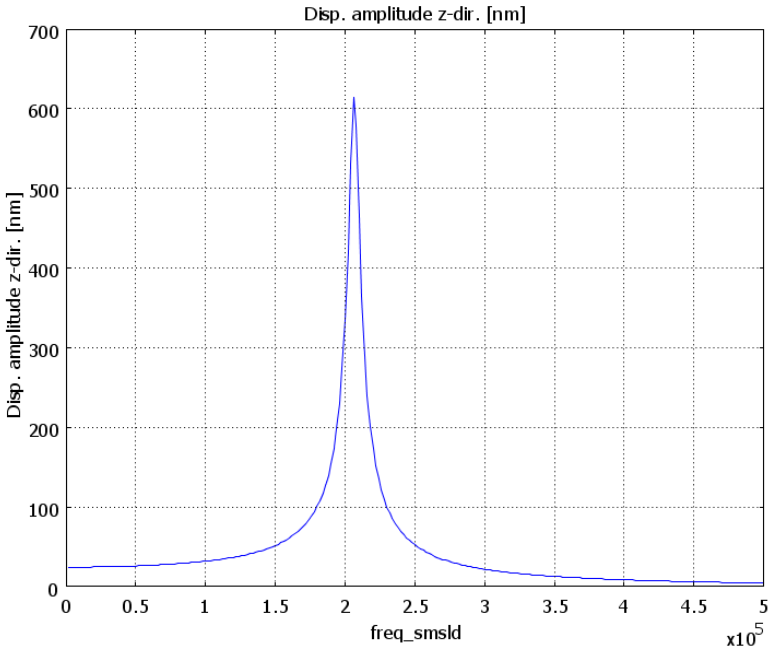

Figure 3.10. Frequency response of the resonator with 6 μm grating period and 30 μm supporting beam length.

bandwidth is calculated as

$$d_{min} = 20\frac{fm}{\sqrt{Hz}} \times \sqrt{500kHz} = 14.14pm(rms) = 20pm(peak) \tag{3.4}$$

This value is 225 times smaller than the smallest mechanical signal for 1 mA peak AC current and 3 T magnetic field strength. This means that we can drive the resonator structures with much smaller current values and still obtain detectable mechanical signal.

After designing three diffraction grating resonators with different grating periods, we simulated the same structures for 0.5 μm and 2 μm metal thickness values. We used the same top view geometry in order to be able to use one mask set with different metal film thickness options. The results can be seen in Table 3.4. Note that minimum displacement values, which are given for 1 kHz to 500 kHz, are again much larger than the detectible smallest displacement value.

Table 3.4. Simulation results for different film thickness values.

Simulation No.	**1**	**2**	**3**	**4**	**5**	**6**
Grating Period (μm)	4	5	6	4	5	6
Film Thickness (μm)	0.5	0.5	0.5	2	2	2
Resonant Frequency (kHz)	94	102	102	378	406	412
Disp. Amp. at Resonance (nm)	1387	1457	1260	396	389	262
Min. Displacement Amplitude (nm)	6.8	5.2	5.5	2.7	3.1	4.1

After finishing the simulations for three main types of resonators, which are determined by grating period; we applied two varieties to these structures. These varieties are both optional and independent from each other. The first one is the split-beam option as in Figure 3.11. The idea is exactly the same as in the case of LDV compatible resonators, which is explained in Section 2.3.

Another option is adding an extra electrical connection to the reflective surface on

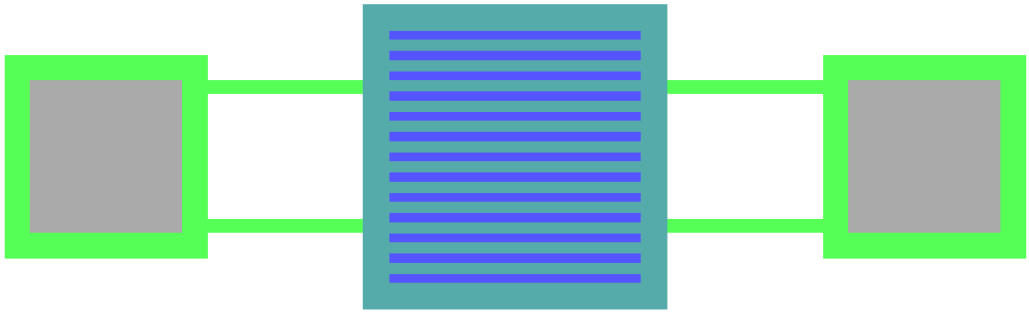

Figure 3.11. Split-beam diffraction grating resonator.

the substrate. Although our actuation mechanism does not require such a connection, we added this option in order to be able to use electrostatic actuation if we desire in the future. The modified layout can be seen in Figure 3.12.

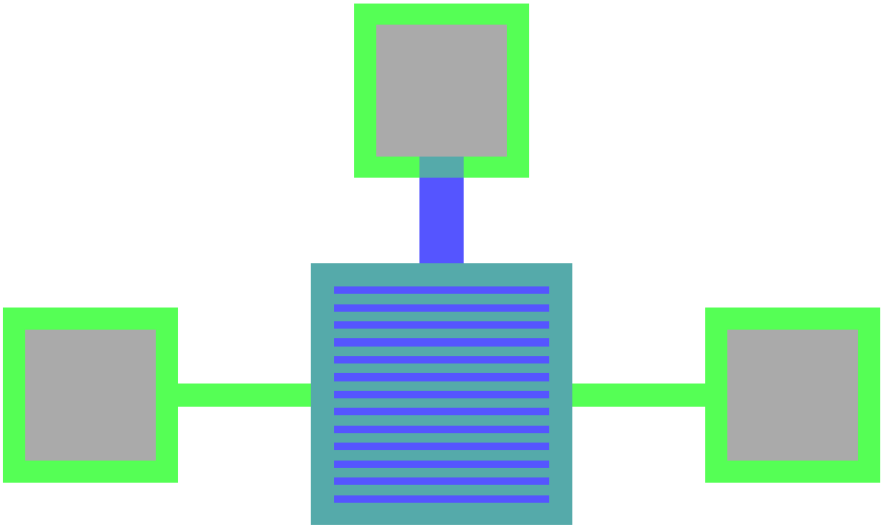

Figure 3.12. Resonator with extra electrical connection option.

4. FABRICATION

In this chapter, we are going to be dealing with the fabrication of the devices that we have designed. This chapter is divided into two sections. The first one explains the proposed fabrication method and design of the masks according to it. The second one investigates the fabrication process in clean-room step by step and addresses particular challenges along with the solutions to them.

4.1. Proposed Method and Design of Masks

As it is explained in Chapters 2 and 3, our resonators are released structures which are anchored to the substrate at the end of two supporting beams. In addition to this, our diffraction grating resonators have an extra reflective surface, a mirror, which lies on the substrate, just beneath the central mass of the resonators. In order to fabricate devices with this level of complexity, we proposed a method which utilizes three masks; specifically for mirrors, anchors, and resonator structures. Figure 4.1 summarizes the fabrication steps.

Since our actuation mechanism requires current flow through the resonators and the force is proportional with the current level, we chose glass as the substrate material in order to prevent leakage because of its insulating characteristic. The first step of the fabrication is defining mirrors under diffraction gratings via standard lift-off process (Figure 4.1a). Since lift-off requires non-conformal metal coating, we decided to use negative photoresist, which results in a more appropriate edge profile for this kind of a process [45]. Figure 4.2 shows the suitable clear field mask for a diffraction grating resonator. After the first lithography step, the fabrication continues with deposition of a thin Al layer using sputtering technique (Figure 4.1b) and the lift-off process (Figure 4.1c).

The aim of the second mask is defining anchors for resonator structures. Because strong anchors require conformal metal deposition, we decided to use positive photore-

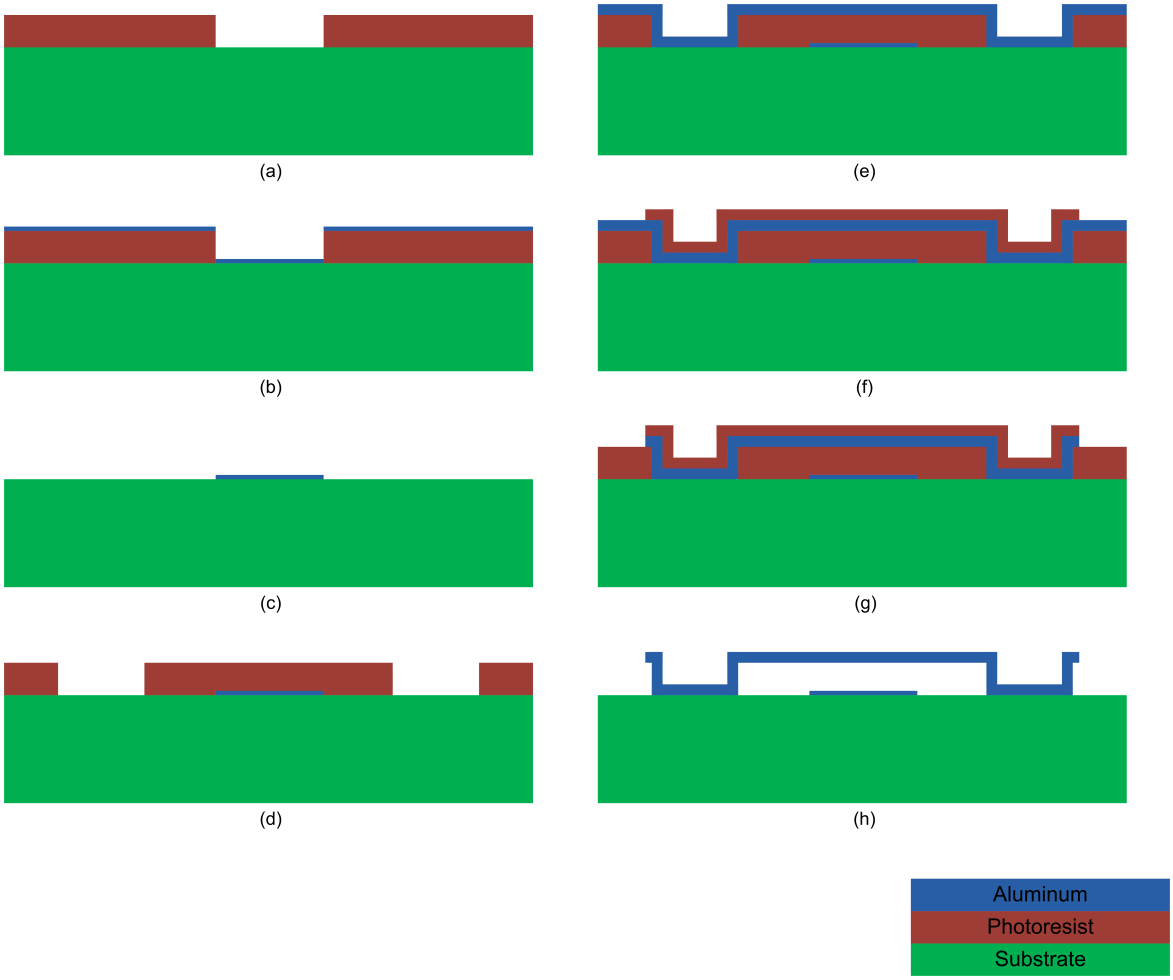

Figure 4.1. Proposed fabrication sequence. (a) Lithography 1. (b) Deposition 1. (c) Lift-off. (d) Lithography 2. (e) Deposition 2. (f) Lithography 3. (g) Wet etching. (h) Releasing.

Figure 4.2. Mask 1 – The Mirror Mask (clear field).

sist for this case in contrast to the previous one. Another difference from the previous case is the polarity of the mask. Figure 4.3 shows the suitable dark field mask for the second lithography step (Figure 4.1d). Note that the squares represent the anchors and they correspond to glass part of the mask instead of the chromium one.

Figure 4.3. Mask 2 – The Anchor Mask (dark field).

The following step is the second Al deposition using sputtering technique, as in Figure 4.1e. This layer is relatively thicker than the previous one and intended to be conformal, since it forms the resonator structures. A third lithography step (Figure 4.1f) defines the protective photoresist layer for the following wet etching step. The photoresist is again positive and Figure 4.4 shows the corresponding clear field mask. Note that the protective layer is formed not only on the released parts of the resonators but also on the anchors. All three masks and their alignment with one another can be seen in Figure 4.5.

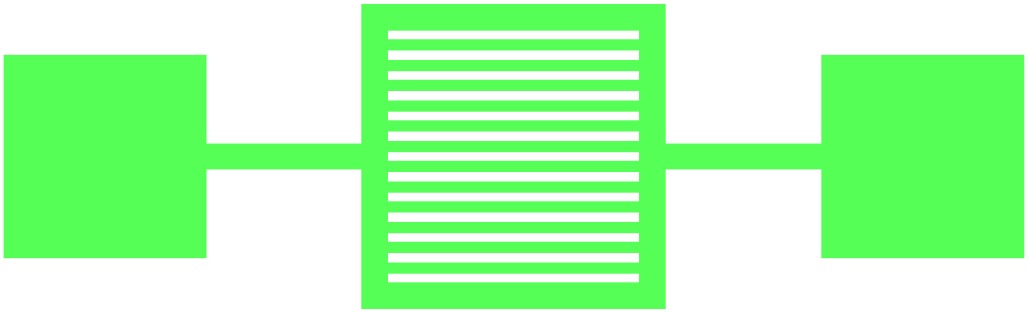

Figure 4.4. Mask 3 – The Structural Mask (clear field).

The process continues with the wet etching of Al to shape MEMS resonators, as in Figure 4.1g. The final step is releasing the structures via plasma etching procedure (Figure 4.1h). Both the sacrificial and the protective photoresist layers are cleaned

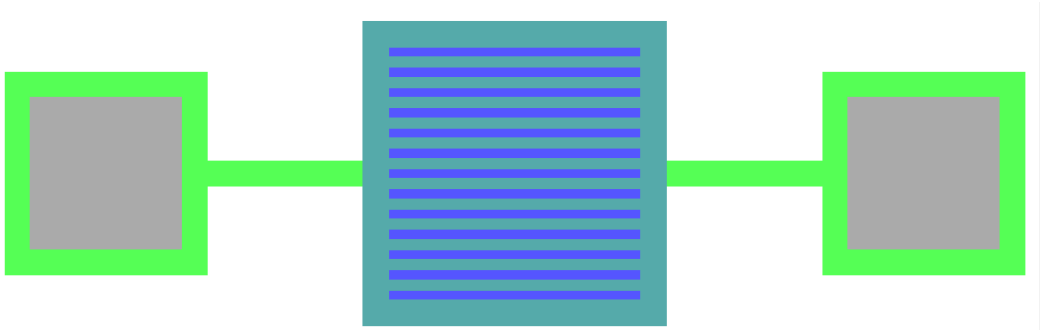

Figure 4.5. Complete layout for a diffraction grating resonator.

during this step. The advantage of using a dry etching technique for releasing structures over acetone cleaning is that the former one does not cause stiction as the latter one [46].

One extra point about the mask design is that the first mask covers anchor parts in addition to mirrors. This is not required for the process; however, it gives us an opportunity to deposit some other type of a metal to the anchor regions as a thin adhesive layer before depositing the second structural metal. This does not cause problem for the mirror region, because the type of the metal does not matter as long as the light is reflected from the surface.

This section summarized the proposed fabrication procedure and appropriate mask design for it. Now, we are going to continue with the realization of the process in clean-room.

4.2. Fabrication Process in Cleanroom

Fabrication of MEMS devices is a complex procedure and many parameters should be optimized to obtain a good result. It is sometimes necessary to repeat some critical steps to find the right parameters. In this section, we are going to explain the process by giving the final parameters. The whole process is performed in the clean-room facility of Center for Life Sciences and Technologies at Boğaziçi University.

The first stage of the fabrication is a lithography process with the mirror mask (Figure 4.1a). We began with spin coating of hexamethyldisilazane (HMDS) with the spin rate of 6000 rpm for 60 seconds. After that, we decreased the rate to 4000 rpm while keeping duration the same to coat AZ 5214 photoresist with 1.4 μm thickness. Next, we soft baked the sample at 110°C for 50 seconds on hot plate as recommended in the datasheet of the photoresist. For exposure, we used EVG620 Automated Mask Alignment System in our cleanroom with soft contact mode and constant dose of 40 mJ/cm^2.

As we mentioned in Section 4.1, this lithography step should be performed using a negative photoresist. AZ 5214 is a special type of a photoresist, which can be used both as a positive and a negative one. If the sample is developed after the exposure step, AZ 5214 acts as a regular positive photoresist. Using it as a negative one requires two extra steps. Since we wanted to do so in this case; after the first exposure, we applied image reversal bake at 120°C for 120 seconds on hot plate and then exposed the sample with constant dose of 175 mJ/cm^2, without any masks. As a result of the image reversal bake, the pre-exposed parts, which are normally soluble in developer solution, become hardened and insoluble even after the second exposure. On the other hand, the other parts, which are not exposed in the first exposure, are not affected by this process and due to the second exposure; they become soluble in developer solution. This is how the image reversing is achieved. Finally, after these two extra steps, we developed the sample using AZ 726 mif developer for 60 seconds.

The second stage of the fabrication is the Al deposition for the mirrors, as shown in Figure 4.1b. For this task, we used Vaksis Angora Sputtering System in our cleanroom. The process was run at 100 W DC power for 30 minutes in order to deposit Al film with 100 nm thickness. Although evaporation is a more appropriate method than sputtering for lift-off process [46], the ratio of photoresist to film thickness is high enough, around 14 in this case, to ensure a good result.

After the metal deposition stage, we proceeded with the third one, which is the lift-off process (Figure 4.1c). We used acetone to etch photoresist and applied

ultrasonic agitation to remove unwanted metal films from the sample. The result can be seen in Figure .

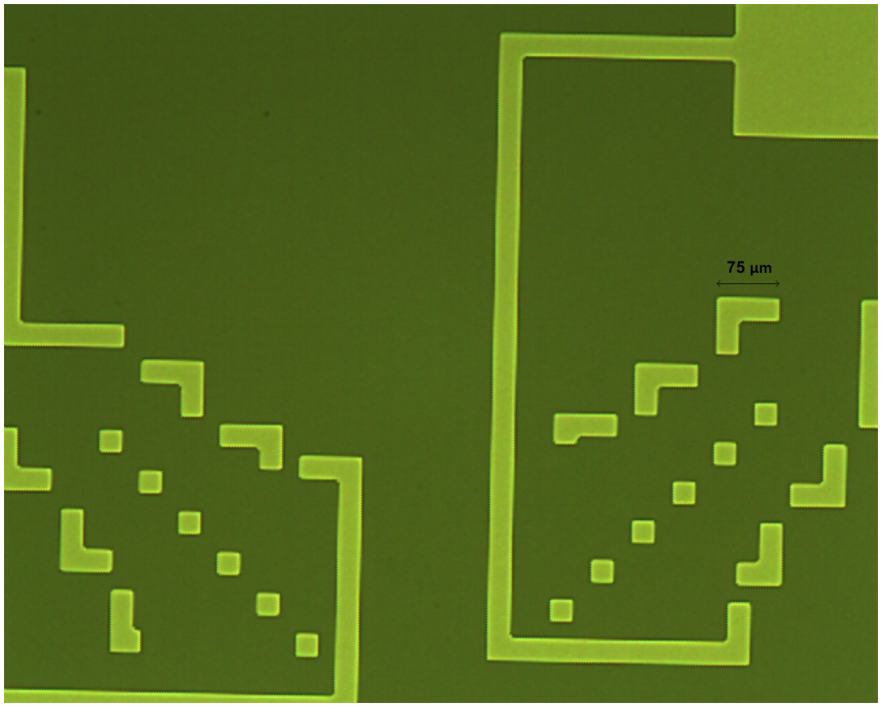

Figure 4.6. Microscopy image after the lift-off process.

The fourth stage is defining the anchor points for resonator structures with a second lithography step (Figure 4.1d). We spin coated HMDS with the same parameters. On the other hand, we decreased the spin rate to 2000 rpm for photoresist coating in order to achieve 2 μm sacrificial layer thickness, which determines the gap between the resonators and the substrate. Duration and the type of photoresist were the same. After soft baking the sample at 110°C for 50 seconds on hot plate, we exposed it with constant dose of 60 mJ/cm^2 in the soft-contact mode. Since this second lithography is a positive photoresist process, we directly continued with the development with AZ 726 mif developer for 85 seconds.

After defining the anchors, we deposited Al layer for resonator structures (Figure 4.1e). We again used sputtering technique with 100 W DC power. This time the duration was increased to 150 minutes to achieve 0.5 μm film thickness.

The sixth stage of fabrication, which is the third lithography process (Figure 4.1f), is one of the most critical ones, because it defines the resonator structures, which are far more detailed than the mirrors and anchors. Especially, diffraction gratings with period of 4 μm, as seen in Figure 4.7, were very hard to define and required many repetitions to optimize process parameters.

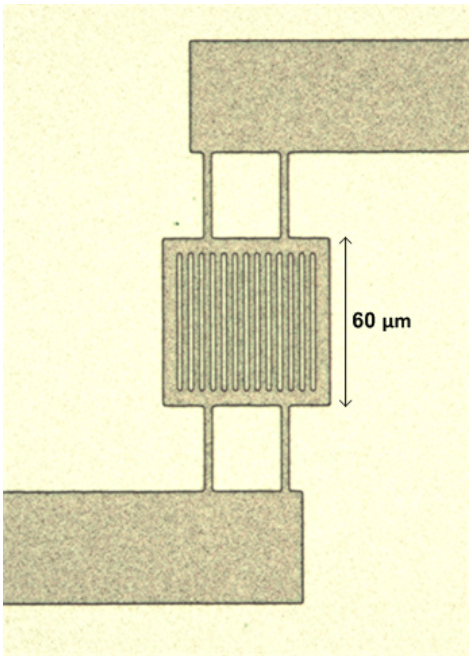

Figure 4.7. Microscopy image of diffraction grating resonator with 4 μm grating period after the third lithography stage.

We again started by spin coating HMDS as in the previous cases. Due to the fact that we were dealing with smaller structures, we span AZ 5214 photoresist with a higher rate, 5000 rpm, in order to obtain a thinner photoresist layer of 1.25 μm thickness. Then, we soft baked the sample at 110°C for 50 seconds on hot plate. For the exposure, we used constant dose of 40 mJ/cm^2 in the hard-contact mode. The reason why we did not use the soft-contact mode in this case is that it did not result in a uniform exposure throughout the wafer. The results were actually very good in the outer parts of the wafer; nevertheless, the same thing was not true for the central parts, because of the very small but finite upwards curvature of the wafer. In order to make the surface as flat as possible during the exposure, we operated the system

in the hard-contact mode. Finally, we performed the development step using AZ 726 mif developer for 70 seconds. Another result for this stage can be seen in Figure 4.8.

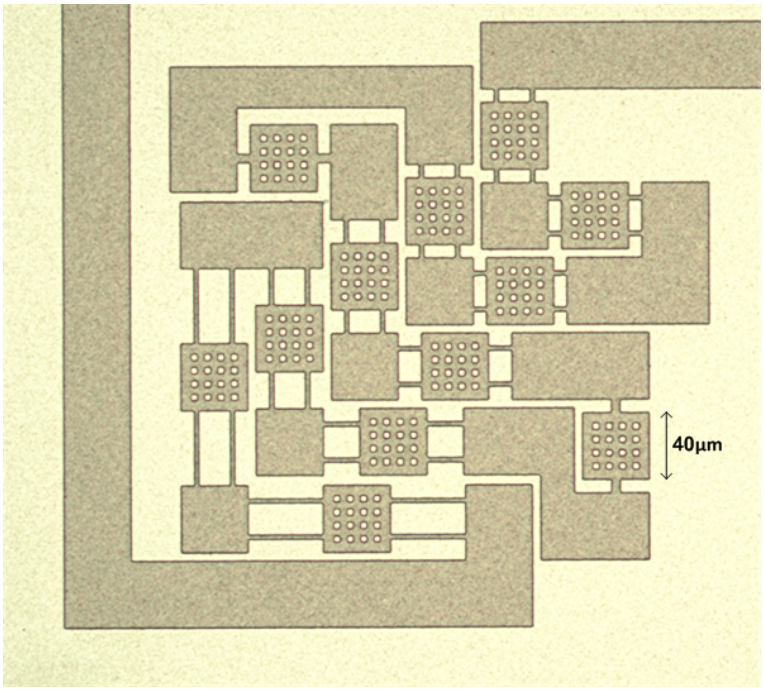

Figure 4.8. Microscopy image of a resonator family after the third lithography stage.

Another very critical stage of fabrication is the wet etching of aluminum for shaping the resonators (Figure 4.1f). The reason why it is critical is that it is a time dependent process. Unless the process is stopped as soon as the unwanted metal is removed, the parts which are supposed to be protected by the photoresist layer continue to be etched. This is especially important for narrow structures, such as beams and diffraction gratings.

As the aluminum etchant, we used the mixture of phosphoric acid (H_3PO_4), nitric acid (HNO_3), acetic acid (CH_3COOH), and DI water [47,48]. The volume percentages of each component for this etchant are 73.0 %, 3.1 %, 3.3 %, and 20.6 %, respectively. Etch rate was around 200 nm/min starting at room temperature. However, it is hard to find an exact rate; since the reaction is exothermic and it becomes faster with increased temperature.

One very important problem with this process is that the hydrogen bubbles that are formed during the reaction cover the surface and diminish the speed of etching. These are especially effective in narrow crevices; therefore, they cause spatial inhomogeneity in terms of the etch rate. In order to avoid this problem, we applied ultrasonic agitation during the process to remove H_2 bubbles [49], which completely solved it. Figure 4.9 and Figure 4.10 show various microscopy images, which are taken after the wet etching stage.

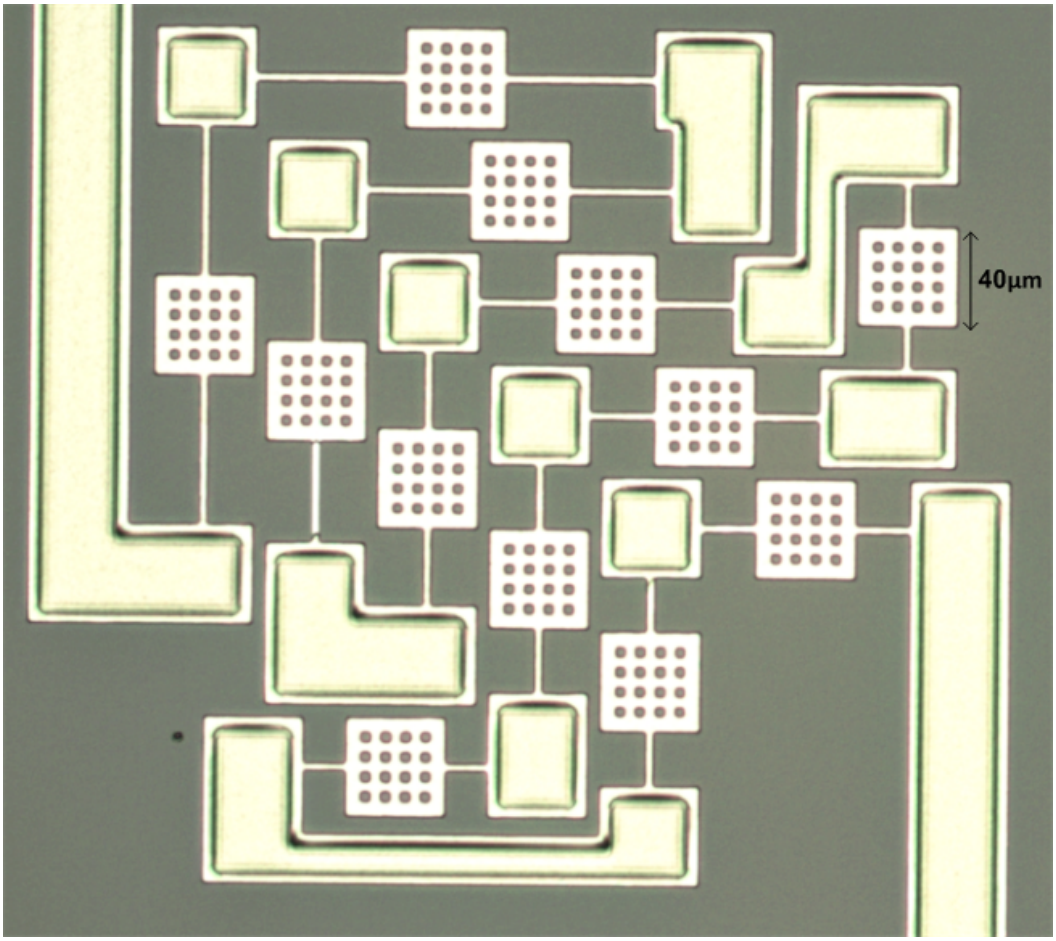

Figure 4.9. Resonator family after the wet etching process.

The final stage of fabrication is plasma etching of remaining photoresist layers (Figure 4.1h). Since our main concern for this stage was to release structures by etching the sacrificial photoresist under the resonators, we needed to achieve an isotropic result. It is possible to use oxygen plasma in both isotropic and anisotropic ways. Oxygen molecule (O_2) turns into two different forms when plasma is formed by RF excitation.

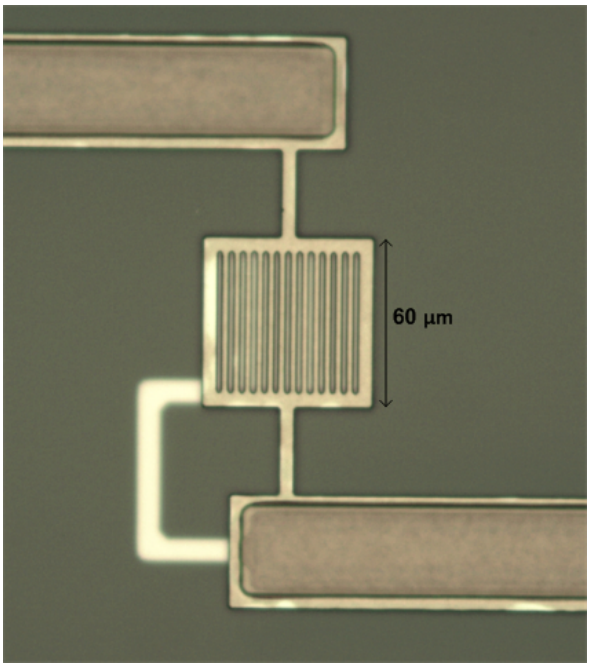

Figure 4.10. Diffraction grating resonator with 4 μm grating period after the wet etching process.

It is either separated into a positively charged ion (O_2^+) ion and a free electron (e^-) or two neutral oxygen radicals (O^*). In the first case, positively charged ions can be accelerated by the electric field and bombard the sample surface, thereby causing a physical etching, which has an anisotropic pattern. In contrast, neutral radicals do not interact with the electric field; however, they are unstable and extremely reactive with certain materials, resulting in a chemical etching, which has an isotropic pattern. In our case, they do react with photoresist but not with aluminum, as it is required.

The pressure of the process determines if it is a chemical or a physical one. For the physical etching, accelerated ions should not collide with each other until they bombard the sample. This requires a relatively long mean free path and can be achieved at low pressure values, which are below 300 mTorr. On the other hand, the chemical etching becomes dominant as the number of radicals increase. The appropriate interval for the pressure value is from 300 mTorr to 1000 mTorr. We used our Nordson March AP-300 Plasma System at 600 mTorr with oxygen for 10 minutes to release the structures and

clean the photoresist layer on the resonators. Figure 4.11 shows a microscopy image taken after this stage.

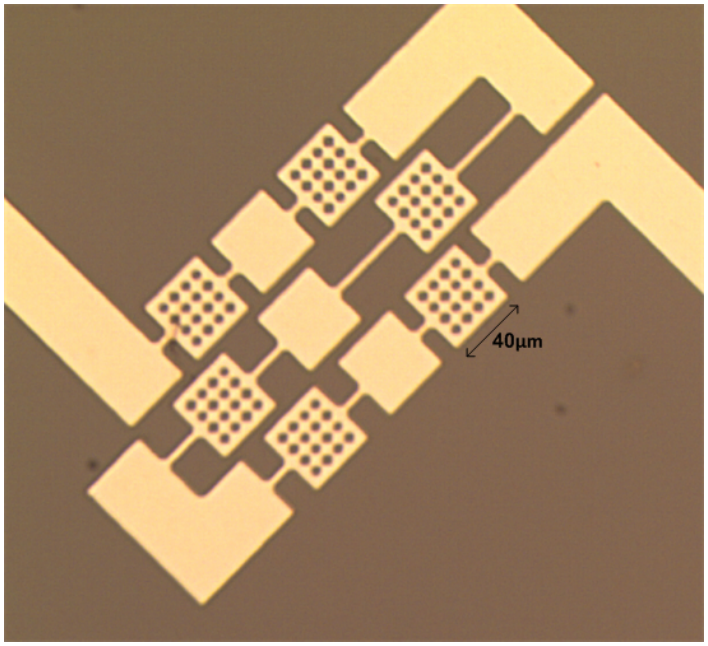

Figure 4.11. Released resonator structures.

5. CHARACTERIZATION

In this chapter we are going to discuss the characterization of our resonator structures. First of all, we will start with the experimental setup and the purpose of each component of it. Then, we will show the frequency response of our devices. Finally, we will investigate the resolution of our measurement.

5.1. Experimental Setup

As shown in Figure 5.1 and Figure 5.2, our experimental setup consists of a vibration isolating optical table (Newport RP Reliance), a function generator (Tektronix AFG 3251C), an oscilloscope (Tektronix TDS 3032B), a spectrum analyzer (Rohde & Schwarz FSV30), a multimeter (Fluke 287), a laser Doppler vibrometer (Polytec OFV-534 Laser Unit and OFV-2500 Vibrometer Controller), contact probes (Cascade Microtech DCM 205 Series), a microscope (Meiji EMZ), a strong permanent magnet, and the device under test.

In order to characterize our devices, AC current is applied to the resonators by the function generator while creating a magnetic field in the perpendicular direction using a permanent magnet. At the same time, we detect the out-of-plane motion using the LDV system. Output of the LDV is fed either to the oscilloscope or the spectrum analyzer depending on the purpose. We use the multimeter in current measurement mode so as to monitor the current through the resonators. In addition, the aim of the contact probes is to provide electrical connection to the devices.

5.2. Frequency Response Measurements

In this section we are going to be demonstrating the dynamic behavior of the resonator structures. By sweeping the frequency of the input current and measuring the corresponding mechanical output, we were able to obtain the transfer function for the devices. We are going to give results for three different micromirror resonators,

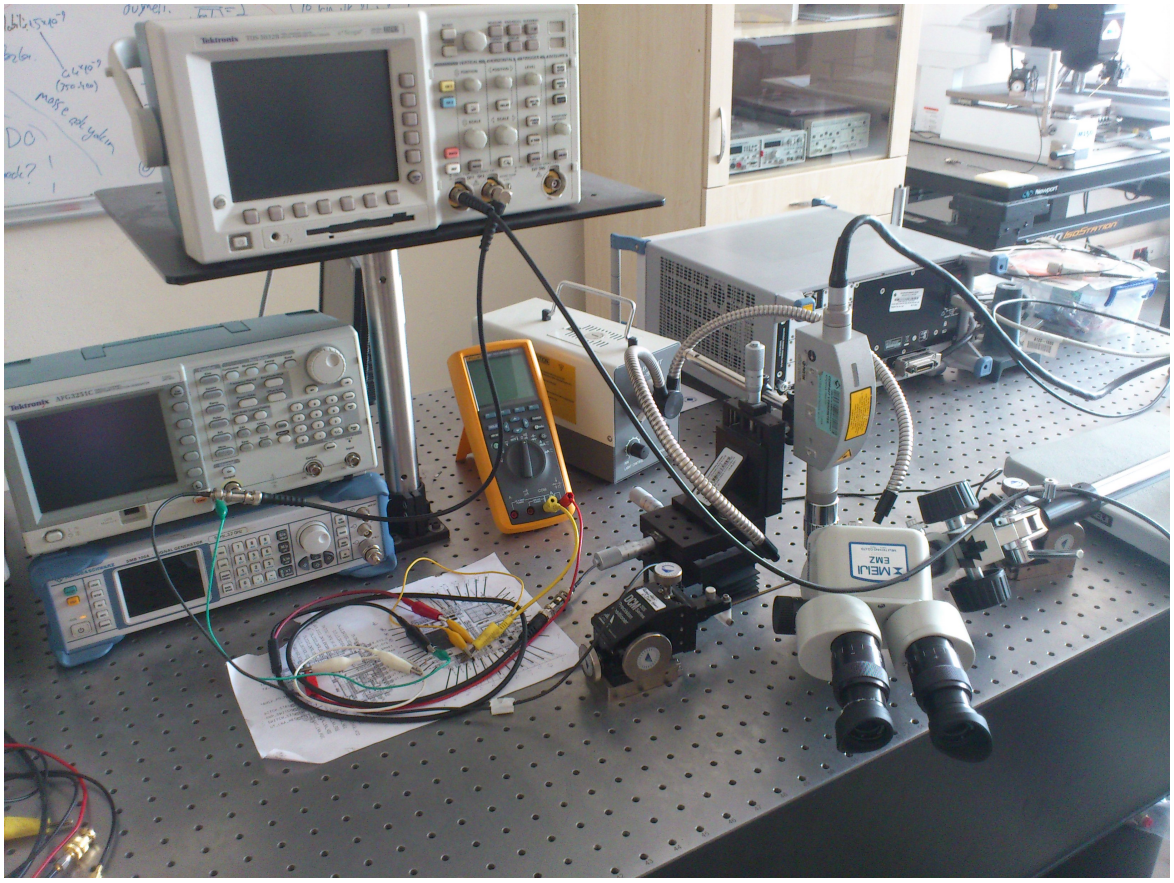

Figure 5.1. Experimental setup: General view.

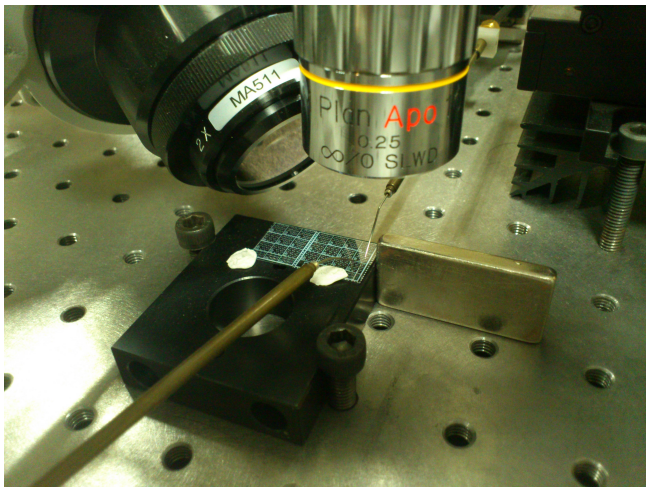

Figure 5.2. The magnet and the device under test.

which differ from each other in terms of their supporting beam lengths that are 45 μm, 16 μm, and 8 μm.

Figure 5.3 shows a typical frequency response curve for a micromirror resonator with 45 μm supporting beam length. In this experiment, the rms value of the driving current is 4 mA and the magnetic field strength is 0.13 T. The results suggest that the resonant frequency of the device is 1075 kHz with a quality factor of 19.55. Although 4 mA rms current is very high for the practical case; we are going to be able to obtain the same mechanical signal with 0.17 mA rms current, since the 3 T magnetic field of clinical-MRI is 23 times stronger than the one in our experiment.

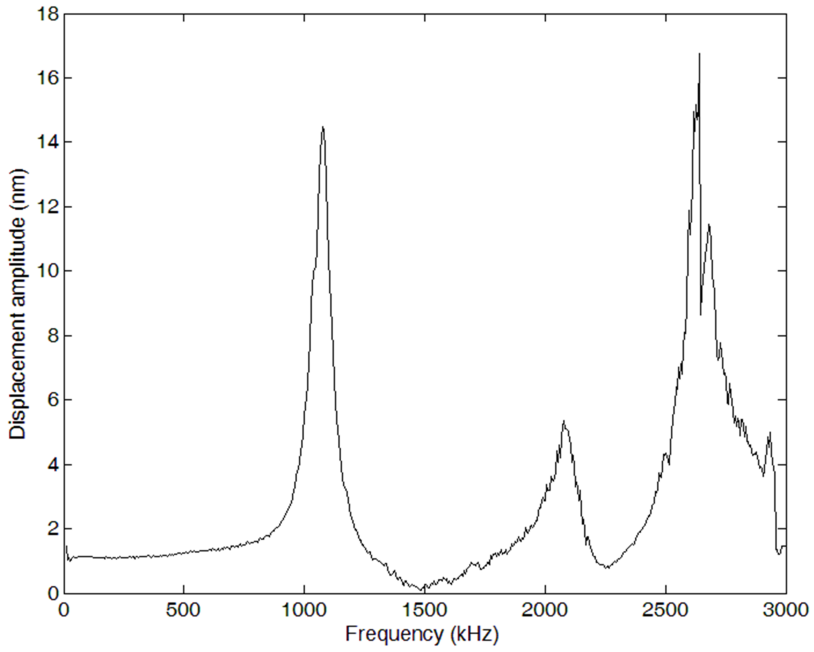

Figure 5.3. Frequency response of micromirror resonator with 45 μm supporting beam length.

The resonant frequency of this particular device according to FEA simulations is 120 kHz. The difference between simulation and experimental results can be explained in terms of the effect of tensile stress (σ_T) on resonant frequency (ω_{res}) [50]. The force (F_T) due to tensile stress (σ_T) that counteracts the out-of-plane displacement of the

central mass can be found as

$$F_T = \sigma_T A \frac{x}{l} \tag{5.1}$$

where A is the cross sectional area of the supporting beam, x is the amount of displacement, and l is the beam length, assuming $x \ll l$. Since there are two supporting beams, the added spring constant (k_T) due to tensile stress is

$$k_T = \frac{2F_T}{x} = \frac{2\sigma_T A}{l} \tag{5.2}$$

The resonant frequency becomes

$$\omega_{\text{res}}^2 = \frac{(k + k_T)}{m} \tag{5.3}$$

$$\omega_{\text{res}}^2 = \frac{2A}{ml^3}\left(Et^2 + \sigma_T l^2\right) \tag{5.4}$$

where m is the mass of the central part and E is the Young's modulus.

The necessary tensile stress value to cause this frequency shift is calculated as 685 MPa, which is high but still reasonable for sputtered Al films [51]. The temperature change (ΔT) for the sputtering process is calculated as 477°K according to Equation 5.5 where α_{Al} is the thermal expansion coefficient for Al (23.1 μm·m^{-1}·K^{-1}) and α_{Si} is that of Si (2.6 μm·m^{-1}·K^{-1}).

$$\sigma_T = E\left(\alpha_{Al} - \alpha_{Si}\right)\Delta T \tag{5.5}$$

We also investigated the behavior of this device for different driving current values at resonance. The dependence of resonant frequency, displacement amplitude, and the quality factor on the input current can be seen in Table 5.1. This analysis shows that,

if we somehow limit our bandwidth of interest around the resonant frequency, we can work with much lower current values than we would normally do.

Table 5.1. Dynamic behavior for different driving current values.

RMS Current	**Disp. Amp. @Resonance**	**Res. Freq.**	**Q Factor**
4.01	15.11	1075	19.55
3.19	12.56	1127	19.74
2.49	9.89	1176	19.48
1.92	7.51	1212	18.58
1.51	6.16	1231	19.35
1.04	4.04	1252	18.96
0.83	3.21	1258	19.05
0.54	2.21	1257	15.26
0.38	1.68	1261	13.56

We conducted the same frequency sweeping experiment with the other micromirror resonators, whose supporting beams are 16 μm and 8 μm long. The magnetic field and the driving current values are again 0.13 T and 4 mA rms. Figure 5.4 and Figure 5.5 show the dynamic behavior of the devices for 16 μm and 8 μm beam lengths, respectively.

Both of the results are qualitatively similar to each other. Firstly, we see the effect of squeeze film damping, because the amplitude declines due to the frequency increase, which causes the air film under the structure to become stiffer. Secondly, we do not see a resonant peak, since it is beyond 3000 kHz, which is the upper limit of our LDV's measurement range. This is an expected result. As we discussed in Section 2.2, resonant frequency is proportional to $l^{-3/2}$, where l is the beam length. Compared to 45 μm devices, this results in 4.72 and 13.34 times higher resonant frequency expectation for 16 μm and 8 μm devices, respectively. Furthermore, squeeze film damping which is dominant at lower frequencies as in this case tends to push the resonant frequency even further as we mentioned in subsection 2.1.2.

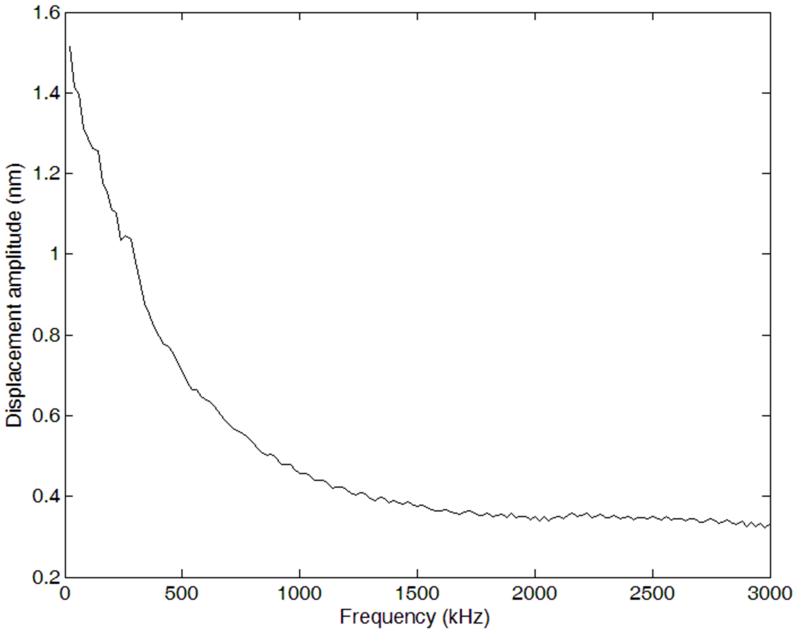

Figure 5.4. Frequency response of micromirror resonator with 16 μm supporting beam length.

5.3. Resolution of the Measurements

In order to be sure that what we measure is a correct result rather than just noise, we have to know the resolution of that measurement. Resolution is a frequency dependent variable and is related with many factors. To measure it, we conducted a simple experiment. While keeping the LDV spot on a micromirror and applying no driving signal, we measured the LDV signal level for different frequencies of interest using the spectrum analyzer. The result can be seen in Figure 5.6.

If we compare this noise floor with the measured values in Section 5.2, we see that the former one is at least 20 times lower than the latter one. Therefore, we can conclude that the previously done measurements are correct, at least from the perspective of noise limitation. One extra point about the noise measurements is that the spectral density of the noise does not depend on the position of the LDV spot, whether it is on the device or on the substrate, as long as the reflected light level is

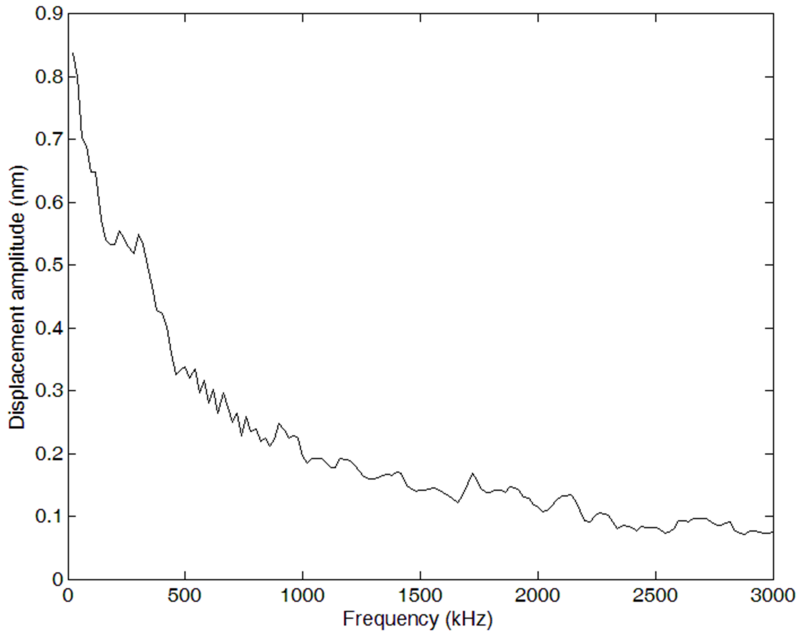

Figure 5.5. Frequency response of micromirror resonator with 8 μm supporting beam length.

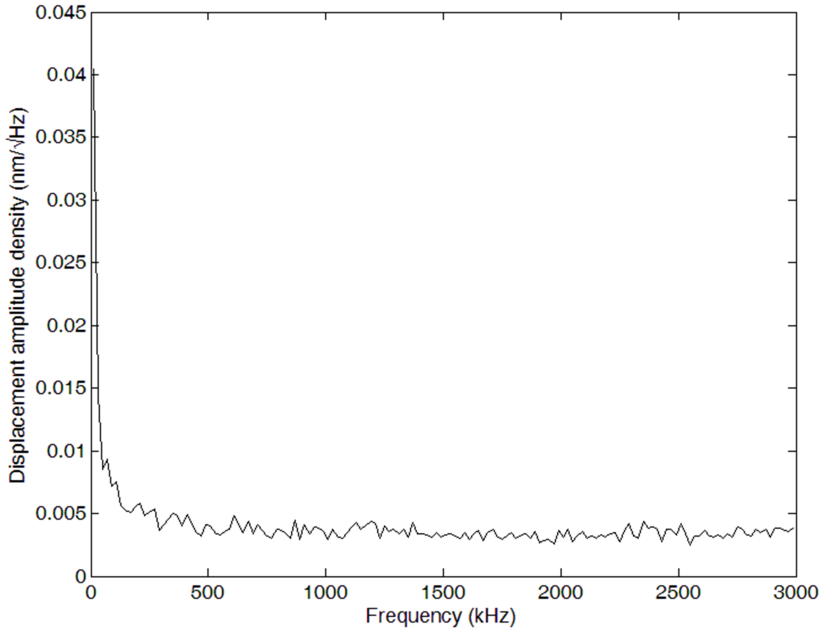

Figure 5.6. Noise floor for the measurement.

the same. In other words, the thermal mechanical noise associated with the devices was dominated by the noise associated with LDV itself. Note that the noise figure of the LDV device depends on the reflected laser intensity.

6. CONCLUSION

In this thesis work, we designed, fabricated, and characterized MEMS resonators for catheter tracking in MRI. The actuation mechanism is based on Lorentz force, which is induced by the interaction of the current driven by an external circuitry at a down-converted frequency and the strong DC magnetic field in the MRI machine. Utilizing the latter one is especially important, since it leads to low-power solutions. The frequency of the produced mechanical signal carries the position information in MRI.

The resonators are designed for two different optical readout methods, which are laser Doppler vibrometry (LDV) and diffraction grating interferometry. For both methods, many different devices are designed for various purposes. Theoretical analysis for the mechanics of the resonator structures, squeeze film air damping, and diffraction grating interferometry are given. Finally, the design approach is verified by using FEA simulations. These simulations include both the mode analysis and the frequency response of the designed resonators. The results show that the minimum displacement amplitude is 4.5 nm in 1 kHz to 500 kHz frequency range, for 1 mA driving current amplitude and 3 T magnetic field strength.

The fabrication is explained in two parts. The first one is the development of an appropriate fabrication procedure and the design of masks according to it. The second and the more challenging part is the process in the cleanroom. As a result, we achieved to fabricate the devices with sufficient quality. We were able to define diffraction gratings with 2 μm grating spacing, which is the hardest part of the devices to fabricate.

After the fabrication, we continued with the characterization of the devices. For the tests, we used a strong permanent magnet to create magnetic field and observed the mechanical output of the resonators using LDV, while they were driven by AC current. Experimental results show that we can indeed actuate the resonators using

Lorentz force. We obtained 15 nm displacement amplitude at resonance for 4 mA rms current and 0.13 T magnetic field strength. Since the product of input current amplitude and the magnetic field strength is comparable with the planned practical case, we are hopeful about having good results in the actual MRI tests.

As a future work, many things should be done for the catheter tracking project as a whole. In addition this, some parts of this thesis work can also be improved. One possible improvement can be done in the fabrication sequence such that the last wet etching step is replaced by an electroplating process. The advantage of this improvement would be the freedom of fabricating a thicker structural metal layer. Since wet etching causes an inevitable undercut, it is not possible to use this method after a certain metal thickness. This is especially important for the diffraction grating resonators. Furthermore, electroplating is a better choice for fabricating stress-free metal films.

One very important work that should be done is to adapt the optical readout methods specifically to our devices and the integration of readout elements with the resonator structures. After this task is accomplished, the integration of the whole microsystem with the medical device must be achieved. It is also very crucial to show that the system actually works in MRI tests.

REFERENCES

1. Yalcinkaya, A. D., "Development of an Electromagnetic MEMS Based, Interventional MRI Compatible Real-Time Localization Microsystem with All-Optical Communication", Project Proposal for TUBITAK, 2011.

2. Kleinerman, R. S., "Cancer Risks Following Diagnostic and Therapeutic Radiation Exposure in Children", *Pediatric Radiology*, Vol. 36, No. 2, pp. 121–125, 2006.

3. Andreassi, M., L. Ait-Ali, N. Botto, S. Manfredi, G. Mottola and E. Picano, "Cardiac Catheterization and Long-Term Chromosomal Damage in Children with Congenital Heart Disease", *European Heart Journal*, Vol. 27, No. 22, pp. 2703–2708, 2006.

4. Vlaardingerbroek, M. T. and J. A. den Boer, *Magnetic Resonance Imaging : Theory and Practice*, Springer, Heidelberg, 2003.

5. Webster, J. G., *Minimally Invasive Medical Technology*, Taylor&Francis, Boca Raton, 2010.

6. Placidi, G., *MRI: Essentials for Innovative Technologies*, Taylor&Francis, Boca Raton, 2012.

7. Yang, X. and E. Atalar, "Intravascular MR Imaging-Guided Balloon Angioplasty with an MR Imaging Guide Wire: Feasibility Study in Rabbits", *Radiology*, Vol. 217, No. 2, pp. 501–506, 2000.

8. Dion, Y. M., H. B. E. Kadi and C. Boudoux, "Endovascular Procedures Under Near-Real-Time Magnetic Resonance Imaging Guidance: An Experimental Feasibility Study", *Journal of Vascular Surgery*, Vol. 32, No. 5, pp. 1006–1014, 2000.

9. Wacker, F. K., C. Hillenbrand and D. R. Elgort, "MR Imaging-Guided Percuta-

neous Angioplasty and Stent Placement in a Swine Model: comparison of Open- and Closed-Bore Scanners", *Academic Radiology*, Vol. 12, No. 9, p. 1085, 2005.

10. Fink, C., M. Bock and R. Umathum, "Renal Embolization: Feasibility of Magnetic Resonance-Guidance Usin Active Catheter Tracking and Intraarterial Magnetic Resonance Angiography", *Investigative Radiology*, Vol. 39, No. 2, pp. 111–119, 2004.

11. Raval, A. N., J. D. Telep and M. A. Guttman, "Real-Time Magnetic Resonance Imaging-Guided Stenting of Aortic Coarctation with Commercially Available Catheter Devices in Swine", *Circulation*, Vol. 112, No. 5, pp. 699–706, 2005.

12. Raval, A. N., P. V. Karmarkar and M. A. Guttman, "Real-Time MRI-Guided Endovascular Recanalization of Chronic Total Arterial Occlusion in a Swine Model", *Circulation*, Vol. 113, No. 8, pp. 1101–1107, 2005.

13. Van Der Laan, M. J., C. J. Bakker and J. D. Blankensteijn, "Dynamic CE-MRA for Endoleak Classification after Endovascular Aneurysm Repair", *European Journal of Vascular and Endovascular Surgery*, Vol. 31, No. 2, pp. 130–135, 2006.

14. Schella, S., M. Saeed and C. B. Higgins, "Magnetic Resonance-Guided Cardiac Catheterization in a Swine Model of Atrial Septal Defect", *Circulation*, Vol. 108, No. 15, pp. 1865–1870, 2003.

15. Lederman, R. J., M. A. Guttman and D. C. Peters, "Catheter-Based Endomyocardial Injection with Real-Time Magnetic Resonance Imaging", *Circulation*, Vol. 105, No. 11, pp. 1282–1284, 2002.

16. Buecker, A., E. Spuentrup and R. Grabitz, "Magnetic Resonance-Guided Placement of Atrial Septal Closure Device in Animal Model of Patent Foramen Orale", *Circulation*, Vol. 106, No. 4, pp. 511–515, 2002.

17. Rickers, C., M. Jerosch-Herold and X. Hu, "Magnetic Resonance Image-Guided

Transcatheter Closure of Atrial Septal Defects", *Circulation*, Vol. 107, No. 1, pp. 132–138, 2003.

18. Schella, S., M. Saeed and C. B. Higgins, "Balloon Sizing and Transcatheter Closure of Acute Atrial Septal Defects Guided by Magnetic Resonance Fluoroscopy: Assessment and Validation in a Larga Animal Model", *Journal of Magnetic Resonance Imaging*, Vol. 21, No. 3, pp. 204–211, 2005.

19. Kuehne, T., S. Yilmaz and C. Meinus, "Magnetic Resonance Image-Guided Transcatheter Implantation of Prosthetic Valve in Aortic Valve Position: Feasibility Study in Swine", *Journal of American Collage of Cardiology*, Vol. 44, No. 11, pp. 2247–2249, 2004.

20. Dickfield, T., R. Kato and M. Zviman, "Characterization of Radiofrequency Ablation Lesions with Gadolinium-Enhanced Cardiovascular Magnetic Resonance Imaging", *Journal of American Collage of Cardiology*, Vol. 47, No. 2, pp. 370–378, 2006.

21. Susil, R. C., C. J. Yeung and H. R. Halperin, "Multifunctional Interventional Devices for MRI: A Combined Electrophysiology/MRI Catheter", *Magnetic Resonance in Medicine*, Vol. 47, No. 3, pp. 594–600, 2002.

22. Lardo, A. C., E. R. McVeigh and P. Jumrussirikul, "Visualization and Temporal/Spatial Characterization of Cardiac Radiofrequency Ablation Lesions Using Magnetic Resonance Imaging", *Circulation*, Vol. 102, No. 6, pp. 698–705, 2000.

23. Arepally, A., P. V. Karmarkar and C. Weiss, "Magnetic Resonance Image-Guided Trans-Septal Puncture in a Swine Heart", *Journal of Magnetic Resonance Imaging*, Vol. 21, No. 4, pp. 463–467, 2005.

24. Kee, S. T., A. Ganguly and B. L. Daniel, "MR-Guided Transjugular Intrahepatic Portosystemic Shunt Creation with Use of a Hybrid Radiography/MR System", *Journal of Vascular and Interventional Radiology*, Vol. 16, No. 1, pp. 227–234,

2005.

25. Arapally, A., P. V. Karmarkar and C. Weiss, "Percutaneous MR Imaging-Guided Transvascular Access of Mesenteric Venous System: Study in Swine Model", *Radiology*, Vol. 238, No. 1, pp. 113–118, 2006.

26. Shellock, F. G., "Radiofrequency Energy-Induced Heating During MR Procedures: A Review", *Journal of Magnetic Resonance Imaging*, Vol. 12, No. 1, pp. 30–36, 2000.

27. Yeung, C. J., R. C. Susil and E. Atalar, "RF Safety of Wires in Interventional MRI: Using a Safety Index", *Magnetic Resonance in Medicine*, Vol. 47, No. 1, pp. 187–193, 2002.

28. Konings, M. K., L. W. Bartels, H. F. M. Smits and C. J. G. Bakker, "Heating Around Intravascular Guidewires by Resonating RF Waves", *Journal of Magnetic Resonance Imaging*, Vol. 12, No. 1, pp. 79–85, 2000.

29. Nyenhuis, J. A., S. M. Park and R. Kamondetdacha, "MRI and Implanted Medical Devices: Basic Interactions with an Emphasis on Heating", *IEEE Transactions on Device and Materials Reliability*, Vol. 5, No. 3, pp. 467–480, 2005.

30. Shellock, F. G., *Magnetic Resonance Procedures: Health Effects and Safety*, CRC Press, Boca Raton, 2001.

31. Bushong, S. C., *Magnetic Resonance Imaging: Physical and Biological Principles*, Mosby, St. Louis, 2003.

32. Bao, M.-H., *Analysis and Design Principles of MEMS Devices*, Elsevier, London, 2005.

33. Newell, W., "Miniaturization of Tuning Forks", *Science*, Vol. 161, No. 1, pp. 1320–1326, 1968.

34. Veijola, T., H. Kuisma, J. Lahdenpera and T. Ryhanen, "Equivalent Circuit Model of the Squeezed Gas Film in a Silicon Accelerometer", *Sensors and Actuators A*, Vol. 48, No. 1, pp. 239–248, 1995.

35. Basak, S., A. Raman and S. V. Garimella, "Hydrodynamic Loading of Microcantilevers Vibrating in Viscous Fluids", *Journal of Applied Physics*, Vol. 99, No. 1, pp. 447–456, 2006.

36. Nayfeh, A. H. and M. I. Younis, "A new approach to the modeling and simulation of flexible microstructures under the effect of squeeze-film damping", *Journal of Micromechanics and Microengineering*, Vol. 12, No. 2, p. 170, 2004.

37. Bao, M. and H. Yang, "Squeeze film air damping in MEMS", *Sensors and Actuators A*, Vol. 136, No. 1, pp. 3–27, 2007.

38. Vemuri, S., G. Fedder and T. Mukherjee, "Low order square film model for simulation of MEMS devices", *International Conference on Modeling and Simulation of Microsystems*, p. 205–208, San Diego, USA, 2000.

39. Veijola, T., A. Pursula and P. Raback, "Extending the validity of squeezed-film damper models with elongations of surface dimensions", *Journal of Micromechanics and Microengineering*, Vol. 15, No. 1, pp. 1624–1636, 2005.

40. Agrawala, A. and S. V. Prabhu, "Survey on measurement of tangential momentum accommodation coefficient", *Journal of Vacuum Science & Technology A*, Vol. 26, No. 4, pp. 634–645, 2008.

41. Lee, W., N. A. Hall, Z. Zhou and F. L. Degertekin, "Fabrication and Characterization of a Micromachined Acoustic Sensor with Integrated Optical Readout", *IEEE Journal of Selected Topics in Quantum Electronics*, Vol. 10, No. 3, pp. 643–651, 2004.

42. Amm, D. T. and R. W. Corrigan, "Grating Light Valve Technology: Update and

Novel Applications", *Society for Information Display Symposium*, Anaheim, USA, 1998.

43. Hall, N. A., W. Lee and F. L. Degertekin, "Capacitive Micromachined Ultrasonic Transducers with Diffraction-Based Integrated Optical Displacement Detection", *IEEE Transactions on Ultrasonics, Ferroelectrics, and Frequency Control*, Vol. 50, No. 11, pp. 1570–1580, 2003.

44. Udd, E., *Fiber Optic Sensors: An Introduction for Engineers and Scientists*, Wiley, New York, 1991.

45. Plummer, J. D., M. Deal and P. D. Griffin, *Silicon VLSI Technology: Fundamentals, Practice, and Modeling*, Prentice Hall, New Jersey, 2000.

46. Senturia, S. D., *Microsystem Design*, Kluwer Academic Publishers, Boston, 2001.

47. Williams, K. and R. Muller, "Etch Rates for Micromachining Processing", *Journal of Microelectromechanical Systems*, Vol. 5, No. 4, pp. 256–269, 1996.

48. Williams, K., K. Gupta and M. Wasilik, "Etch Rates for Micromachining Processing: Part II", *Journal of Microelectromechanical Systems*, Vol. 12, No. 6, pp. 761–778, 2003.

49. MicroChemicals GmbH, *Lithography Trouble Shooter: Questions and Answers Around the Most Common Problems in Micro-Structuring*, Germany, 2012.

50. Wylde, J. and T. J. Hubbard, "Elastic Properties and Vibration of Micro-Machined Structures Subject to Residual Stresses", *IEEE Canadian Conference on Electrical and Computer Engineering*, pp. 1674–1679, Edmonton, Canada, 1999.

51. Chinmulgund, M., R. Inturi and J. Barnard, "Effect of Ar Gas Pressure on Growth, Structure, and Mechanical Properties of Sputtered Ti, Al, TiAl, and Ti_3Al Films", *Thin Solid Films*, Vol. 270, No. 1, pp. 260–263, 1995.